Dual topological insulator with mirror symmetry protected helical edge states

Warlley H. Campos, ^{1,2}, * Poliana H. Penteado, ^{1,3} Julian Zanon, ⁴ Paulo E. Faria Junior, ⁵ Denis R. Candido, ⁶ and J. Carlos Egues ^{1,3}

¹ Instituto de Física de São Carlos, Universidade de São Paulo, 13560-970 São Carlos, São Paulo, Brazil
 ² Institut für Physik, Johannes Gutenberg-Universität Mainz, 55099 Mainz, Germany
 ³ Department of Physics, University of Basel, Klingelbergstrasse 82, CH-4056 Basel, Switzerland
 ⁴ Department of Applied Physics and Science Education,
 Eindhoven University of Technology, 5612 Eindhoven AZ, Netherlands
 ⁵ Institut für Theoretische Physik, Universität Regensburg, D-93040 Regensburg, Germany
 ⁶ Department of Physics and Astronomy, University of Iowa, Iowa City, Iowa 52242, USA

Dual topological insulators (DTIs) are simultaneously protected by time-reversal and crystal symmetries, representing advantageous alternatives to conventional topological insulators. By combining ab initio calculations and the $k \cdot p$ approach, here, we investigate the electronic band structure of a Na₂CdSn triatomic layer and derive a low-energy 4×4 effective model consistent with all the symmetries of this material class. We obtain the effective Hamiltonian using the Löwdin perturbation theory, the folding-down technique, and the theory of invariants and determine its parameters by fitting our analytical dispersion relations to those of ab initio calculations. We then calculate the bulk topological invariants of the system and show that the Na₂CdSn triatomic layer is a giant-gap (hundreds of millielectronvolts) quasi-two-dimensional DTI characterized by both spin and mirror Chern numbers -2. In agreement with the bulk-boundary correspondence theorem, we find that a finite-width strip of Na₂CdSn possesses two pairs of counterpropagating helical edge states per interface. We obtain analytical expressions for the edge state energy dispersions and wave functions, which are shown to agree with our numerical calculations. Our work opens an avenue for further studies of Na₂CdSn as a potential DTI candidate with room-temperature applications in areas of technological interest, such as nanoelectronics and spintronics.

I. INTRODUCTION

Since the theoretical proposal and experimental observation of two-dimensional (2D) [1-6] and threedimensional (3D) [7–12] topological insulators (TIs), these materials have been the subject of substantial research in condensed matter physics and related areas of science [11, 13–17]. Further investigations soon resulted in the discovery of another important class of topological materials named topological crystalline insulators (TCIs) [18–22]. Both TIs and TCIs host midgap boundary states related to a bulk topological invariant via the bulk-boundary correspondence [23, 24]. The TI phase can be characterized by a nontrivial spin Chern number (in 2D) [25–28] or \mathbb{Z}_2 invariant [1, 3, 8], whereas the characterization of a TCI phase depends on the material and involves at least one crystal symmetry, e.g., inversion, rotation, or the mirror operation [it may or may not involve time-reversal symmetry (TRS)]. Well-known examples are TCIs characterized by the mirror Chern number [20, 29–31] and the Z_2 invariant defined in terms of the product of time reversal with a C_4 rotation [18].

The interplay between time-reversal and crystalline symmetries on the topology of 3D materials was investigated in $\mathrm{Bi}_{1-x}\mathrm{Sb}_x$ [32, 33] and $\mathrm{Bi}_2\mathrm{Te}_3$ [34] alloys, which were predicted to be not only Z_2 TIs but also TCIs characterized by a nontrivial mirror Chern number. Such a dual topological character defines $\mathrm{Bi}_{1-x}\mathrm{Sb}_x$, $\mathrm{Bi}_2\mathrm{Te}_3$, and

other materials [35–39] as dual TIs (DTIs), considered more robust against external perturbations than each constituent phase [34, 36, 40]. For example, it has been shown that, to open a gap in the Dirac cone describing the (111) surface states of Bi₂Te₃, one must break time-reversal and mirror symmetries simultaneously [34].

DTIs in 2D have been much less studied than their 3D counterparts. The literature is nearly limited to theoretical studies of the Na₃Bi single-layer system [41–43]. More recently, the rectangular Bi bilayer [40] and the hexagonal IrO [44] have also been proposed. Up to now, to the best of our knowledge, these have not yet been experimentally realized.

In this paper, we explore an overlooked DTI constituted by a triatomic layer of the ternary sodium compounds Na_2XY (X = Mg, Cd; Y = Pb, Sn), which can potentially be obtained by mechanical exfoliation of 3D van der Waals Dirac semimetals [45] already synthesized experimentally [46, 47]. We derive a $\mathbf{k} \cdot \mathbf{p}$ Hamiltonian for this class of materials (provided that the ordering of the energy bands around the Fermi level is the same as that for Na₂CdSn) and analyze the bulk topology and the corresponding mirror symmetry protected helical edge states of its Na₂CdSn representative. By carrying out density functional theory (DFT) calculations, we first obtain the electronic band structure of Na₂CdSn, including the irreducible representations (irreps), orbital composition, and spin texture of the energy bands (Fig. 1). Then we derive our 4×4 model Hamiltonian for the Na₂XY material class by employing group theory analysis and three techniques well established in the $k \cdot p$ literature, namely, the

^{*} Corresponding author: warlleyhcampos@gmail.com

Löwdin perturbation theory [48, 49], the folding-down approach [50–52], and the theory of invariants [49, 53].

To obtain the parameters of our model, we diagonalize our effective Hamiltonian and fit its analytical energy dispersions to our DFT results. We then investigate the orbital (pseudospin) composition and spin texture of the effective band structure (Fig. 2). As a consequence of mirror symmetry [54] (see Appendix A), the energy bands are spin polarized along the z direction, in agreement with the DFT calculations (Fig. 1). Furthermore, by regularizing our model and numerically evaluating the Chern number [55] for each spin sector, we show that Na₂CdSn is a DTI with the TI and TCI phases characterized by spin and mirror Chern numbers -2, respectively (Fig. 3).

We investigate the DTI spectrum for two finite systems: a semi-infinite plane (vacuum/DTI) and a ribbon geometry (vacuum/DTI/vacuum). For the semi-infinite plane, we employ the envelope function approach to analytically derive two pairs of counterpropagating topological edge states related by TRS (Kramers pairs) whose dispersion relations depend quadratically on the crystal momentum (Fig. 4). For the ribbon geometry, we use the finite difference method to numerically obtain its electronic band structure and identify the existence of four pairs of counterpropagating edge states, two pairs located on each interface of the system (Fig. 5). The states localized at opposite sides of the ribbon are quasidegenerate, with a small spin splitting caused by the bulk inversion asymmetry (BIA). Our results for both geometries are in agreement with the bulk-boundary correspondence theorem [23, 24].

The extra robustness against external perturbations [34, 36, 40] positions DTIs as promising materials for applications in nanotechnology. The Na₂CdSn system investigated here is even more compelling. According to our DFT calculations, its expected bulk energy gap, $E_g \approx 234.8 \,\mathrm{meV}$, is $\sim 1 \,\mathrm{order}$ of magnitude larger than those of 2D TIs based on HgTe/CdTe, InAs/GaSb or InAs_{0.85}Bi_{0.15}/AlSb quantum wells, for which $E_g \lesssim 30 \,\mathrm{meV}$ [6, 56–58]. Such features showcase this ternary compound as an outstanding candidate for the study of room-temperature topological effects and the development of nanoelectronic [59–61], spintronic [62–64], thermoelectric [65–67], and optical [68, 69] devices.

We note that a study of the Na₂XY triatomic layers was performed in Ref. [70]. The authors propose an effective model Hamiltonian ¹ that can be immediately seen to differ from ours by (i) the lack of terms proportional to $(k_x \pm ik_y)^2$ in the off-diagonal matrix elements and (ii) the presence of terms proportional to $k_x \pm ik_y$ in the secondary diagonal, where $\mathbf{k} = (k_x, k_y)$ represents

the crystal momentum. It is important to emphasize that we consistently kept terms up to second order in k in the perturbation theory.

As we discuss in Sec. IV, the terms proportional to $(k_x \pm ik_y)^2$ play a crucial role in the calculation of the spin and mirror Chern numbers, which are both equal to -2. Moreover, they give rise to the quadratic energy dispersions of the corresponding topological edge states. The topological invariants obtained from our analytical model differ significantly from the spin and mirror Chern numbers -1 reported in Ref. [70]. Following the bulk-boundary correspondence theorem, we predict the existence of two pairs of helical edge states at each boundary of a finite Na₂XY system, whereas Ref. [70] reports only a single pair.

To ensure the accuracy of our model, we first performed the derivation of the $k \cdot p$ Hamiltonian using the Löwdin perturbation theory, and separately, using the folding-down approach. We also derived our effective Hamiltonian using the theory of invariants. The results obtained are in complete agreement with each other and differ from the model proposed in Ref. [70]. In addition, our investigation here goes beyond that of Ref. [70] by providing effective $k \cdot p$ parameters for the Na₂CdSn DTI and deriving analytical expressions for both the energy dispersion and wave functions of the edge states arising in this material.

This paper is organized as follows. In Sec. II, we present the crystal structure and DFT calculations for Na_2CdSn triatomic layers. Section III is devoted to the $k \cdot p$ model obtained via the Löwdin perturbation theory. We also present our results regarding the fitting of the effective model to the energy bands obtained via DFT. In Sec. IV, we analyze the topology of Na_2CdSn , and in Sec. V, we calculate the analytical dispersion relations for the topological edge states. We also present our numerical study of the topological edge states in a ribbon geometry. We summarize our findings in Sec. VI.

II. Na₂CdSn TRIATOMIC LAYER: CRYSTAL STRUCTURE AND DFT RESULTS

The Na₂CdSn triatomic layer is constituted by Cd and Sn atoms forming a coplanar hexagonal lattice, while the sodium (Na) atoms lie above and below the center of each hexagon, forming a quasi-2D honeycomb material (see Fig. 1). This quasi-2D structure can be found as the constituting stacking block of the 3D Na₂CdSn Dirac semimetal, already synthesized experimentally [46, 47]. In recent first-principles calculations, Mao *et al.* [70] have verified the stability of these compounds by performing phonon spectrum analysis and revealing only positive phonon energies.

In Fig. 1-a), we show a top view of the Na₂CdSn. The coordinate system is chosen such that the z axis points out of the plane of the figure. The primitive lattice vectors read $\mathbf{a}_1 = \frac{a}{2} (\sqrt{3}, 1)$ and $\mathbf{a}_2 = (0, a)$, where a

¹ The authors of Ref. [70] provide very limited information about the basis set used in their work. This precluded us from verifying whether their reported effective Hamiltonian respects all the symmetries of the system – in particular time-reversal symmetry.

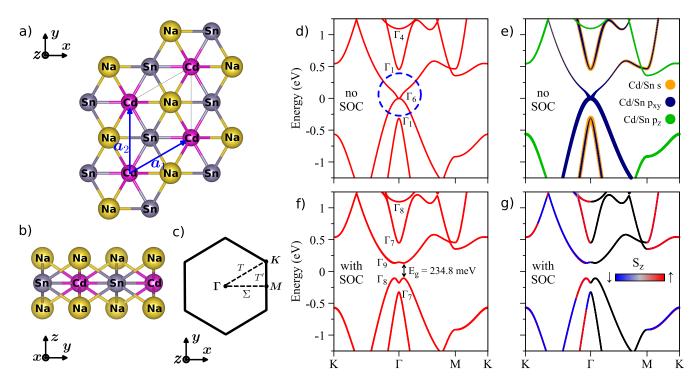


Figure 1. (Color online) a) Top and b) side views of the quasi-two-dimensional (2D) honeycomb crystal structure of Na₂CdSn. The Cd and Sn atoms crystallize in a hexagonal lattice, while Na atoms lie above and below the center of each hexagon. The coordinate system used is shown according to the respective view. c) Brillouin zone (BZ) for the quasi-2D honeycomb crystal structure. $\Gamma = (0,0), M = \frac{2\pi}{\sqrt{3}a}(1,0), \text{ and } K = \frac{2\pi}{3a}(\sqrt{3},1), \text{ where } a \text{ is the lattice constant.}$ The $\Gamma - M, \Gamma - K, \text{ and } M - K$ high-symmetry lines are labeled by Σ , T, and T', respectively. d) Electronic band structure of Na₂CdSn without spin-orbit coupling (SOC). The two Γ_6 bands are degenerate at the Fermi level ($E_F = 0$), characterizing a semimetal. The region of interest, to be described by the effective model, is indicated by the blue dashed circle. e) Orbital composition of the band structure without SOC. The Γ_6 bands (close to E_F) are dominated by the p_x and p_y orbitals (dark blue) of Cd and Sn, while the Γ_1 bands are dominated by the s orbital. f) When SOC is considered, a gap of $E_g = 234.8$ meV opens up at the Fermi level, and we can see that the material is a semiconductor. Furthermore, the energy bands are spin degenerate along the Γ_1 high-symmetry line but present a very small spin splitting along the other directions. g) Spin texture of the electronic band structure with SOC. The energy bands have spin expectation value of $\langle S_z \rangle \approx \pm \hbar/2$ [$\langle S_z \rangle > 0$ ($\langle S_z \rangle < 0$) red (blue)], while $\langle S_x \rangle = \langle S_y \rangle = 0$. The doubly degenerate bands along $\Gamma - M$ are colored black, for $\langle S_z \rangle$ is not univocally defined along this direction.

is the lattice parameter. In Fig. 1-b), we show a side view of the crystal structure with the observer looking from the positive x axis. From this angle, the x axis points out of the plane of the figure, and we can see more clearly the position of the Na atoms relative to Cd and Sn. The reciprocal lattice vectors can be shown to be $\mathbf{b}_1 = \left(\frac{4\pi}{\sqrt{3}a},0\right)$ and $\mathbf{b}_2 = \frac{2\pi}{\sqrt{3}a}\left(-1,\sqrt{3}\right)$. The first Brillouin zone (BZ) in this coordinate system is shown in Fig. 1-c), along with the high-symmetry points $\Gamma = (0,0), M = \left(\frac{2\pi}{\sqrt{3}a},0\right)$ and $K = \frac{2\pi}{3a}\left(\sqrt{3},1\right)$ [71].

The crystal structure of the 3D bulk compound belongs to the nonsymmorphic space group D_{6h}^4 (P_{63}/mmc), with point group D_{6h} (6/mmm) [45, 47, 72–74]. Our DFT results show that the Na₂CdSn triatomic layer belongs to the D_{3h}^1 ($P\bar{6}m2$) space group, whose crystallographic point group is D_{3h} ($\bar{6}m2$) [47, 72]. The corresponding set of generators are the C_3 rotation about the z axis (C_{3z}), C_2 rotation about the x axis (C_{2x}), and

the mirror plane reflection about the xy plane (σ_h) [see character table in the Supplemental Material (SM) [75] (see also Refs. [76–78] therein)].

We investigate the electronic structure of Na₂CdSn using DFT as implemented in the WIEN2k package [79], a full potential all-electron code employing the linearized augmented plane-wave plus local orbitals method. We use the Perdew-Burke-Ernzerhof (PBE) exchange-correlation functional [80], a Monkhorst-Pack k-grid of 15×15, and self-consistent convergence criteria of 10^{-6} e (elementary charge) for the charge and 10^{-6} Ry for the energy. We consider a core-valence separation energy of -6 Ry, atomic spheres with orbital quantum numbers up to 10, and the plane-wave cutoff multiplied by the smallest atomic radii is set to 8. In the absence of spin-orbit coupling (SOC), we optimize the structural parameters and obtain an in-plane lattice parameter $a = 4.978 \,\mathrm{A}$ and a thickness (vertical distance between Na atoms) of 3.332 Å (consistent with the lattice

parameters of the 3D bulk compound [45, 46]). In the SM [75] we present the total energy obtained within DFT as a function of the lattice parameter a and thickness d. In the presence of SOC, core electrons are considered fully relativistically, whereas valence electrons are treated in a second variational step [81], with the scalar-relativistic wave functions calculated in an energy window of -10 to 4 Ry. We consider a vacuum region of $20 \,\text{Å}$.

In Figs. 1-d) and 1-e), we show the electronic band structure and the orbital composition, respectively, obtained via DFT calculations for Na₂CdSn in the absence of SOC. The Fermi level (E_F) lies at zero energy, and the blue dashed circle indicates the low-energy region we are interested in. The band structure is that of a semimetal with two Γ_6 bands fourfold degenerate at the Γ point (accounting for the twofold spin degeneracy of each band). The closest remote bands belong to the Γ_1 and Γ_4 irreps [75]. We note that the Γ_6 bands are dominated by the p_x and p_y orbitals of the Cd and Sn atoms [dark blue in 1-e)], while the Γ_1 bands are dominated by s orbitals (yellow) with a minor contribution from p_x and p_y (for more details, see SM [75]).

In the presence of SOC, Fig. 1-f), the degeneracy at the Γ point is lifted, and an energy gap $E_g=234.8\,\mathrm{meV}$ opens up. The material then becomes a semiconductor with topmost valence bands belonging to the Γ_7 and Γ_8 irreps, while the lowest conduction bands belong to Γ_7 and Γ_9 . The next remote conduction band belongs to the Γ_8 irrep. All irreps are obtained from the total wave function

In Fig. 1-g), we show the expectation value of the z component of spin (color coded) $\langle \hat{S}_z \rangle$ [$\langle \hat{S}_z \rangle > 0$ ($\langle \hat{S}_z \rangle < 0$) red (blue)]. We note that along the $\Gamma - M$ high-symmetry line (Σ), all energy bands are doubly degenerate. This high-symmetry line belongs to the point group C_{2v} , whose double group has only one irrep – the 2D Σ_5 [82]. The spin-up and down components of the electron wave functions transform according to the two basis functions of Σ_5 . Therefore, all energy bands must be spin degenerate along this direction. Since any linear combination of the spin-degenerate states is also an eigenstate of the Hamiltonian, $\langle \hat{S}_z \rangle$ is not univocally defined along $\Gamma - M$. Hence, we represent the degenerate bands using the black color.

The $\Gamma-K$ (T) and M-K (T') lines, on the other hand, belong to the point group C_s , which consists of only two elements: the identity and the mirror symmetry σ_h . Its double group representation has two one-dimensional (1D) irreps, T_3 (T_3') and T_4 (T_4') for spin-up and -down states, respectively, along the T (T') line. Thus, the energy bands are spin split along these directions. The spin expectation values of all eigenstates out of the $\Gamma-M$ line are given by $\langle \hat{S}_z \rangle \approx \pm \hbar/2$ and $\langle \hat{S}_x \rangle = \langle \hat{S}_y \rangle = 0$, as required by mirror symmetry about the z direction (see Appendix A) [54]. We note that our DFT calculated band structure is in great agreement with the previous report of Mao $et\ al.$ [70].

Based on our DFT calculations, in the next section, we

focus on the derivation of an effective model to describe the electronic states close to E_F around the Γ point.

III. THE EFFECTIVE $k \cdot p$ MODEL

Following the approach adopted by Liu et al. [11], we apply the $k \cdot p$ method together with perturbation theory to derive an effective low-energy Hamiltonian for the quasi-2D Na₂CdSn (for details, see SM [75]). Our final 4×4 model describes the four energy bands close to E_F around the Γ point $[\Gamma_8$ and Γ_9 bands in Fig. 1-f)].

The general $\mathbf{k} \cdot \mathbf{p}$ Hamiltonian around the Γ point is given by [49]

$$\mathcal{H}(\mathbf{k}) = \epsilon(\mathbf{k}) + \mathcal{H}_0 + \mathcal{H}_{\mathbf{k} \cdot \mathbf{p}} + \mathcal{H}_{so} + \mathcal{H}_{\mathbf{k}so}, \tag{1}$$

where \mathbf{k} is the crystal momentum and $\epsilon(\mathbf{k}) = \frac{\hbar^2 k^2}{2m_0}$, with $k = |\mathbf{k}|$, \hbar the reduced Planck constant, and m_0 the bare electron mass. The second term in Eq. (1),

$$\mathcal{H}_0 = \frac{\mathbf{p}^2}{2m_0} + V(\mathbf{r}),\tag{2}$$

corresponds to the Hamiltonian at $\mathbf{k} = 0$ in the absence of SOC, with $\mathbf{p} = -i\hbar \nabla$ the linear momentum operator and $V(\mathbf{r})$ the effective single-particle crystal potential. The $\mathbf{k} \cdot \mathbf{p}$ and \mathbf{k} -independent SOC terms read, respectively,

$$\mathcal{H}_{\boldsymbol{k}\cdot\boldsymbol{p}} = \frac{\hbar}{m_0} \boldsymbol{k} \cdot \boldsymbol{p},\tag{3}$$

and

$$\mathcal{H}_{so} = \frac{\hbar}{4m_0^2 c^2} \mathbf{A} \cdot \hat{\boldsymbol{\sigma}},\tag{4}$$

with $\mathbf{A} = \nabla V \times \mathbf{p}$, c the speed of light, and $\hat{\boldsymbol{\sigma}} = (\hat{\sigma}_x, \hat{\sigma}_y, \hat{\sigma}_z)$ the spin operator divided by $\hbar/2$. Finally, the \mathbf{k} -dependent SOC term is given by

$$\mathcal{H}_{\boldsymbol{k}so} = \frac{\hbar^2}{4m_0^2c^2}\boldsymbol{k}\cdot\hat{\boldsymbol{\sigma}}\times\boldsymbol{\nabla}V(\boldsymbol{r}). \tag{5}$$

The perturbative corrections to the $k \cdot p$ Hamiltonian are calculated by including the remote energy bands via Löwdin perturbation theory or the folding-down method. We note that, even though the Löwdin perturbation and folding-down techniques are essentially equivalent, the calculations are performed differently in each case. In the Löwdin approach, we can include all the infinite remote bands in the perturbative corrections of the $k \cdot p$ Hamiltonian up to second order in the crystal momentum. In the folding down, on the other hand, we can only account for a finite number of remote bands.

Next, we show our effective Hamiltonian derived via Löwdin perturbation theory. The derivation via folding down is discussed in detail in the SM [75].

Löwdin perturbation

As mentioned above, here we will focus on the topmost valence and lowest conduction bands at the Γ point and include the remote bands perturbatively up to second order in k (see more details about the Löwdin perturbation theory in the SM [75]). From the DFT results, Fig. 1d), we extract that the bands we are interested in are described by the two basis functions of the Γ_6 irrep. According to the character table of group D_{3h} [75], these eigenstates can be represented by the $|X\rangle$ and $|Y\rangle$ basis functions, which constitute the basis set for the orbital subspace of the truncated Hamiltonian. As usual, we use the eigenstates of the \tilde{S}_z operator, $|\uparrow\rangle$ and $|\downarrow\rangle$, as the basis for the spin subspace. Finally, the four-dimensional spinful basis set is given by the direct product between the basis functions of the spin subspace and those of the orbital subspace, e.g., $|X\uparrow\rangle = |\uparrow\rangle \otimes |X\rangle$.

The expressions for the first-order terms are obtained by projecting the total Hamiltonian [Eq. (1)] onto a truncated basis consisting of eigenstates of \mathcal{H}_0 [Eq. (2)]. The matrix elements of the second-order contributions, on the other hand, are calculated using standard perturbation theory formulas (Eq. (S30) in the SM [75]). In practice, the matrix representation of the second-order contributions is calculated separately and added to the first-order matrix Hamiltonian:

$$H = \epsilon^{(1)}(\mathbf{k}) + H_0^{(1)} + H_{\mathbf{k} \cdot \mathbf{p}}^{(1)} + H_{so}^{(1)} + H_{\mathbf{k} so}^{(1)}$$

$$+ H_{\mathbf{k} \cdot \mathbf{p}}^{(2)} + H_{\mathbf{k} \cdot \mathbf{p}, so}^{(2)} + H_{so, \mathbf{k} \cdot \mathbf{p}}^{(2)}$$

$$+ H_{\mathbf{k} \cdot \mathbf{p}, \mathbf{k} so}^{(2)} + H_{\mathbf{k} so, \mathbf{k} \cdot \mathbf{p}}^{(2)}$$

$$+ H_{so}^{(2)} + H_{so, \mathbf{k} so}^{(2)} + H_{\mathbf{k} so, so}^{(2)} + H_{\mathbf{k} so}^{(2)}.$$

$$(6)$$

Table I. First-order coupling parameters of the $\mathbf{k} \cdot \mathbf{p}$ Hamiltonian in Eq. (6). Left and right columns show the parameters and their expressions, respectively. All parameters are real. ε_{ij3} is the Levi-Civita (permutation) symbol, and repeated indices are summed over, according to the Einstein convention. For more details on the group theory calculations, see Sec. S-V of SM [75].

Parameter	Expression
ϵ_0	$\langle X \mathcal{H}_0 X angle$
α	$-\hbar^2 \left\langle X \varepsilon_{ij3} \partial_i V \partial_j Y \right\rangle / \left(4m_0^2 c^2 \right)$
ζ	$\hbar^2 \left\langle X \partial_x V X \right\rangle / \left(4m_0^2 c^2\right)$

Projecting each term of Eq. (1) onto the basis $\{|X\uparrow\rangle$, $|Y\uparrow\rangle$, $|X\downarrow\rangle$, $|Y\downarrow\rangle$ and employing group theory analysis to find selection rules for the matrix elements (see Sec. S-V in the SM [75]) yields

$$\epsilon^{(1)}(\mathbf{k}) = \epsilon(\mathbf{k})\sigma_0 \otimes \tau_0, \tag{7}$$

$$H_0^{(1)} = \epsilon_0 \sigma_0 \otimes \tau_0, \quad H_{k,n}^{(1)} = 0,$$
 (8)

$$H_{so}^{(1)} = -\alpha \sigma_3 \otimes \tau_2, \tag{9}$$

$$H_{\mathbf{k}so}^{(1)} = \zeta \sigma_3 \otimes (k_x \tau_1 + k_y \tau_3), \qquad (10)$$

where τ_0 (σ_0) and τ_i (σ_i), i = 1, 2, 3, are the 2 × 2 identity and Pauli matrices in the orbital (spin) subspace, respectively. The expressions for the parameters of the first-order terms are provided in Table I.

For the second-order contributions, we have

$$H_{\mathbf{k}\cdot\mathbf{p}}^{(2)} = \frac{1}{2}\sigma_0 \otimes \left[(A_1 + A_2) k^2 \tau_0 + 2 (A_1 - A_2) k_x k_y \tau_1 + (A_1 - A_2) (k_x^2 - k_y^2) \tau_3 \right], \tag{11}$$

$$H_{\mathbf{k}\cdot\mathbf{p},so}^{(2)} + H_{so,\mathbf{k}\cdot\mathbf{p}}^{(2)} = D_1\sigma_3 \otimes (k_x\tau_1 + k_y\tau_3), \qquad H_{\mathbf{k}\cdot\mathbf{p},\mathbf{k}so}^{(2)} + H_{\mathbf{k}so,\mathbf{k}\cdot\mathbf{p}}^{(2)} = Bk^2\sigma_3 \otimes \tau_2, \qquad (12)$$

$$H_{so}^{(2)} = C_1\sigma_0 \otimes \tau_0 - C_2\sigma_3 \otimes \tau_2, \qquad H_{so,\mathbf{k}so}^{(2)} + H_{\mathbf{k}so,so}^{(2)} = E_1\sigma_3 \otimes (k_x\tau_1 + k_y\tau_3), \qquad (13)$$

$$H_{so}^{(2)} = C_1 \sigma_0 \otimes \tau_0 - C_2 \sigma_3 \otimes \tau_2, \qquad H_{so,kso}^{(2)} + H_{kso,so}^{(2)} = E_1 \sigma_3 \otimes (k_x \tau_1 + k_y \tau_3),$$
 (13)

$$H_{\mathbf{k}so}^{(2)} = \frac{1}{2}\sigma_0 \otimes \left[(F_1 + F_2) k^2 \tau_0 + 2 (F_1 - F_2) k_x k_y \tau_1 + (F_1 - F_2) (k_x^2 - k_y^2) \tau_3 \right], \tag{14}$$

with second-order parameters A_1 , A_2 , D_1 , B, C_1 , C_2 , E_1 , F_1 and F_2 given in Appendix B. Note that, here, we have considered the influence of all the remote bands up to second order in k. Equations (8)–(14) are in agreement with our derivation using the theory of invariants (see Appendix C).

The eigenvalues of the Hamiltonian in Eq. (6) at k =**0** read $\tilde{E}_1 = \tilde{E}_3 = C + M$ and $\tilde{E}_2 = \tilde{E}_4 = C - M$, with $C = \epsilon_0 + C_1$ and $M = \alpha + C_2$. The corresponding eigenvectors are given by $|u_{1(2),\mathbf{0}}\uparrow\rangle$ and $|u_{3(4),\mathbf{0}}\downarrow\rangle$ in Table II. Next, we follow a usual procedure in the $k \cdot p$ literature [49, 51, 52] and perform a change of basis from

 $\{|X\uparrow\rangle, |Y\uparrow\rangle, |X\downarrow\rangle, |Y\downarrow\rangle\}$ to $\{|u_{1,\mathbf{0}}\uparrow\rangle, |u_{2,\mathbf{0}}\uparrow\rangle, |u_{3,\mathbf{0}}\downarrow\rangle,$

 $|u_{4,\mathbf{0}}\downarrow\rangle$, rewriting the full \mathbf{k} -dependent Hamiltonian in a simpler form (diagonal at $\mathbf{k}=0$):

$$H(\mathbf{k}) = \begin{pmatrix} C + M - (D+B)k^2 & -iAk_{-} + Gk_{+}^2 & 0 & 0\\ iAk_{+} + Gk_{-}^2 & C - M - (D-B)k^2 & 0 & 0\\ 0 & 0 & C + M - (D+B)k^2 & -iAk_{+} + Gk_{-}^2\\ 0 & 0 & iAk_{-} + Gk_{+}^2 & C - M - (D-B)k^2 \end{pmatrix},$$
(15)

where

$$A = D_1 + E_1 + \zeta, \tag{16}$$

$$D = -\frac{1}{2} \left[(A_2 + A_1) + (F_2 + F_1) + \frac{\hbar^2}{m_0} \right], \qquad (17)$$

and

$$G = \frac{1}{2} \left[(A_2 - A_1) + (F_2 - F_1) \right]. \tag{18}$$

Table II. Truncated set of zone-center wave functions used as the basis of the Hamiltonian in Eq. (15).

Basis function	Expression
$ u_{1,0}\uparrow\rangle$	$\frac{i}{\sqrt{2}}(X\uparrow\rangle - i Y\uparrow\rangle)$
$ u_{2,0}\uparrow\rangle$	$-\frac{i}{\sqrt{2}}(X\uparrow\rangle+i Y\uparrow\rangle)$
$ u_{3,0}\downarrow\rangle$	$-\frac{\sqrt[4]{2}}{\sqrt{2}}(X\downarrow\rangle+i Y\downarrow\rangle)$
$ u_{4,0}\downarrow\rangle$	$\frac{i}{\sqrt{2}}(X\downarrow\rangle - i Y\downarrow\rangle)$

The matrix Hamiltonian in Eq. (15) is block diagonal, with each block corresponding to a different spin. This is in total agreement with the derivation via folding down (Sec. S-V in the SM [75]). Since there is no coupling between these two blocks, the z component of spin is a good quantum number. As we shall see in Sec. III C, the parameter B, arising from the $H_{\mathbf{k}\cdot\mathbf{p},\mathbf{k}so}^{(2)}$ and $H_{\mathbf{k}so,\mathbf{k}\cdot\mathbf{p}}^{(2)}$ terms often neglected for other materials in the literature, is very important for the topology of our system.

Our $\mathbf{k} \cdot \mathbf{p}$ Hamiltonian contains off-diagonal matrix elements Gk_{\pm}^2 (absent in the model of Mao et al. [70]), which are captured by keeping all contributions up to second order in \mathbf{k} in the Löwdin perturbation theory, folding-down technique, or theory of invariants (Appendix C). In addition, the Hamiltonian proposed by Mao et al. [70] has terms linear in k_{\pm} in the secondary diagonal, coupling opposite spins. In our model, any term connecting the two spin subspaces is forbidden by symmetry ². This result was obtained via all the three perturbative approaches considered in this paper.

In the next section, we analyze the symmetries of our effective $\mathbf{k} \cdot \mathbf{p}$ Hamiltonian.

B. Symmetry analysis

The TRS operator $\mathcal{T} = -i\hat{\sigma}_y K$, with K the complex conjugate operator, projected onto the basis $\{|u_{1,\mathbf{0}}\uparrow\rangle, |u_{2,\mathbf{0}}\uparrow\rangle, |u_{3,\mathbf{0}}\downarrow\rangle, |u_{4,\mathbf{0}}\downarrow\rangle\}$ (Table II) is given by $T = -i\sigma_2 \otimes \tau_0 K$. We have verified that our model Hamiltonian in Eq. (15) respects the condition of invariance under TRS by satisfying $TH(\mathbf{k}) T^{-1} = H(-\mathbf{k})$.

The mirror symmetry operator for spinful electrons satisfies [20, 32]

$$\hat{\sigma}_h^2 = -1. \tag{19}$$

Hence the eigenvalues of $\hat{\sigma}_h$ are i and -i. For a 2D crystal invariant under mirror symmetry about the xy-plane, $[\mathcal{H}, \hat{\sigma}_h] = 0$, the eigenstates of the Bloch Hamiltonian can be chosen to also be eigenstates of $\hat{\sigma}_h$ for all crystal momenta k. This yields two classes of Bloch eigenstates with mirror eigenvalues $\eta = \pm i$, important for the calculation of the mirror Chern number (Sec. IV).

Using the basis of our $k \cdot p$ model (Table II), the matrix representation of the mirror symmetry operator reads

$$\sigma_h = -i\sigma_3 \otimes \tau_0 = \begin{pmatrix} -i & 0 & 0 & 0 \\ 0 & -i & 0 & 0 \\ 0 & 0 & i & 0 \\ 0 & 0 & 0 & i \end{pmatrix}. \tag{20}$$

The model Hamiltonian in Eq. (15) satisfies [75]

$$\sigma_h H(\mathbf{k}) \, \sigma_h^{-1} = H(u_{\sigma_h} \mathbf{k}), \qquad (21)$$

where u_{σ_h} is the matrix representation of the mirror operator acting on the coordinate space. Therefore the spin texture of the simultaneous eigenstates of $H(\mathbf{k})$ and σ_h must be polarized along the z direction in the whole 2D BZ, except at degeneracies [see Fig. 1-g) and Appendix A] [54]. An equation analogous to Eq. (21) holds for the remaining symmetry operations of the point group D_{3h} (see SM [75]).

² By applying the theory of invariants using an extended basis set, we have verified that the next remote band, Γ_4 , couples to the bands of interest, Γ_6 , through zeroth- and first-order in k spin-mixing terms. However, after eliminating the remote bands via

Löwdin perturbation theory, the final 4×4 Hamiltonian remains equivalent to Eq. (15), with the new terms merely renormalising the model parameters. This result is in line with our model derivation in Appendix C, where we have obtained all terms allowed by symmetry through the theory of invariants.

Having the final effective Hamiltonian [Eq. (15)] at hand, we now obtain the corresponding energy bands and perform a fitting procedure using the DFT results [see Fig. 1-f)].

C. Fitting

The four energy bands obtained by diagonalizing the Hamiltonian in Eq. (15) are given by

$$E_{1(3),\mathbf{k}} = C - Dk^2 + \sqrt{M^2 + \Delta_{\mp}(\mathbf{k})},$$
 (22)

$$E_{2(4),\mathbf{k}} = C - Dk^2 - \sqrt{M^2 + \Delta_{\pm}(\mathbf{k})},$$
 (23)

where $E_{1,k}$ and $E_{2,k}$ correspond to the spin-up sector, $E_{3,k}$ and $E_{4,k}$ to the spin-down sector, and

$$\Delta_{\pm}(\mathbf{k}) = \pm 2AG \left(-3k_x^2 + k_y^2 \right) k_y + (A^2 - 2MB)k^2 + \left(G^2 + B^2 \right) k^4.$$
 (24)

By fitting the energy bands [Eqs. (22) and (23)] to the band structure obtained via DFT calculations, we obtain numerical values for the model parameters, shown in Table III.

A range of $\sim 5.5\%$ of the $\Gamma-M$ line was used in the fitting performed with the LMFIT package for Python [83]. The LMFIT package provides several minimization methods that usually yield different parameter sets. We followed the iterative procedure used in Ref. [84], where the best parameter set is chosen after an initial fit and used as an input for a new fit using all minimization methods. The best parameter set is chosen again from the new output and this process is repeated until the parameters that reproduce best the DFT data are obtained.

In Table III, we also show the corresponding Hamiltonian terms that contribute to each of the model parameters (see Appendix B for details). For G=0, the Hamiltonian in Eq. (15) resembles the well-known Bernevig-Hughes-Zhang (BHZ) model [5]. In both models, the energy bands are inverted if MB>0, and therefore, the parameter B is important for the topological analysis of the band structures. We notice that the contributions to the parameter B, accounting for all the remote bands perturbatively, come from $H_{\mathbf{k}\cdot\mathbf{p},\mathbf{k}so}^{(2)}+H_{\mathbf{k}so,\mathbf{k}\cdot\mathbf{p}}^{(2)}$, i.e., the second-order contribution via $\mathcal{H}_{\mathbf{k}\cdot\mathbf{p}}$ and $\mathcal{H}_{\mathbf{k}so}$. This suggests that the second-order correction coming from the \mathbf{k} -dependent SOC should not be neglected for Na₂CdSn.

In Fig. 2-a), we show the energy bands using the parameters obtained from the fitting (solid curves) and from DFT calculations (dashed). The color code represents the direction in the BZ, with green and magenta for the high-symmetry lines $\Gamma - M$ and $\Gamma - K$, respectively. As expected, our $\mathbf{k} \cdot \mathbf{p}$ model reproduces well the DFT data around the Γ point but deviates from the numerical data for larger values of the crystal momentum. In addition, note that the energy bands of the analytical model deviate from the DFT bands before they reach the minimum

Table III. Parameters of the model Hamiltonian derived via Löwdin perturbation theory. The second column shows the numerical values obtained from the fitting to the DFT energy bands, while the third column shows which Hamiltonian terms contribute to each parameter.

	Fitting value	Contributions
\overline{C}	$-0.029{\rm eV}$	$H_0; H_{so}^{(2)}$
M	$0.165\mathrm{eV}$	$H_{so}; H_{so}^{(2)}$
A	$0.0199\mathrm{eV}\!\cdot\!\mathrm{Å}$	$H_{\mathbf{k}so}; H_{\mathbf{k}\cdot\mathbf{p},so}^{(2)}; H_{\mathbf{k}so,\mathbf{k}\cdot\mathbf{p}}^{(2)}; H_{\mathbf{k}so,so}^{(2)}; H_{k$
G	$-116\mathrm{eV}{\cdot}\mathrm{\AA}^2$	$H_{oldsymbol{k}oldsymbol{\cdot}oldsymbol{p}}^{(2)}; \dot{H}_{oldsymbol{k}oldsymbol{so}}^{(2)}$
D	$-44.33\mathrm{eV}{\cdot}\mathrm{\AA}^2$	$H^{(2)}_{oldsymbol{k} \cdot oldsymbol{p}}; H^{(2)}_{oldsymbol{k} so}$
B	$47.87\mathrm{eV}{\cdot}\mathrm{\mathring{A}}^2$	$H^{(2)}_{oldsymbol{k}\cdotoldsymbol{p},oldsymbol{k}so,oldsymbol{k}\cdotoldsymbol{p}};H^{(2)}_{oldsymbol{k}so,oldsymbol{k}\cdotoldsymbol{p}}$

and maximum of the conduction and valence bands, respectively. As a result, the energy gap for the fitted parameters $E_g = 285$ meV is $\sim 21\%$ larger than the gap obtained via DFT calculations. This, however, does not affect the topological properties of the material (see Sec. IV).

In Fig. 2-b), we show the spin-up conduction and valence bands $[E_{1,k}]$ and $E_{2,k}$ in Eqs. (22) and (23), respectively] for the fitted parameters with the orbital composition (color code). Note that the conduction band is dominated by the $|X\rangle - i|Y\rangle$ state (brownish red) at the Γ point, while the valence band is dominated by $|X\rangle + i|Y\rangle$ (green). For larger values of the crystal momentum, both states become relevant to the two energy bands.

In Fig. 2-c), we show the four energy bands for the fitted parameters, colored according to their spin texture. The bands are spin degenerate along the $\Gamma-M$ direction, in agreement with the DFT results (see Fig. 1). The spin splitting along the $\Gamma-K$ line, $\Delta E_s \equiv E_{3,k}-E_{1,k}=E_{4,k}-E_{2,k}$, is very small, reaching a maximum of 3 meV in the range shown. In the inset we display ΔE_s as a function of k. Note that this spin splitting is not accompanied by a mixing of the spin components since there is no coupling between spin-up and spin-down blocks in the effective Hamiltonian in Eq. (15). According to Eq. (24), such a spin splitting requires that both parameters A and G be finite.

In the next section, we perform a topological analysis of our effective model and predict that the Na₂CdSn is a DTI characterized by nontrivial topological invariants.

IV. TOPOLOGY ANALYSIS

Our model Hamiltonian in Eq. (15) can be rewritten in the compact form

$$H(\mathbf{k}) = \begin{pmatrix} h(\mathbf{k}) & 0\\ 0 & h^*(-\mathbf{k}) \end{pmatrix}, \tag{25}$$

with $h(\mathbf{k}) = d_0(\mathbf{k})\bar{\tau}_0 + \mathbf{d}(\mathbf{k}) \cdot \bar{\boldsymbol{\tau}}$. The matrices $\bar{\tau}_0$ and $\bar{\boldsymbol{\tau}} = (\bar{\tau}_1, \bar{\tau}_2, \bar{\tau}_3)$ are the identity and Pauli matrices in the basis $\{i(|X\rangle - i|Y\rangle)/2, -i(|X\rangle + i|Y\rangle)/2\}$ of the or-

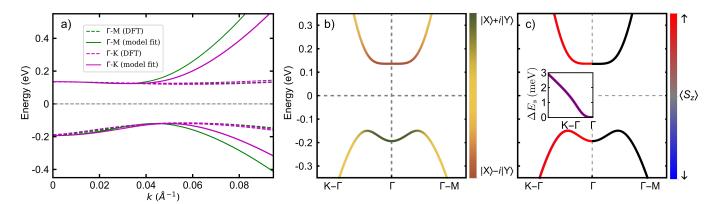


Figure 2. (Color online) Effective energy bands for Na₂CdSn. a) Fitting of the 4×4 model Hamiltonian derived via $k \cdot p$ theory to the density functional theory (DFT) energy bands. A range of $\sim 5.5\%$ of the $\Gamma - M$ line was used in the fitting, whose numerical values of the parameters are given in Table III. Solid (dashed) curves represent the energy bands from the effective model (DFT calculations), and green (magenta) represents the $\Gamma - M$ ($\Gamma - K$) high-symmetry line. (b) Spin-up bands with orbital (pseudospin) composition. The color bar shows the contribution from the $|X\rangle + i|Y\rangle$ (green) and $|X\rangle - i|Y\rangle$ (brownish red) states. (c) The four energy bands of the model (both spins) with spin expectation value. The spin-up bands are colored red, while the spin-down bands are blue. The bands are spin degenerate along the $\Gamma - M$ high-symmetry line. In this case, the spin expectation value is not univocally defined. For this reason, we color the bands black in this direction. Along $\Gamma - K$, there is a spin splitting (not distinguishable in the main graph) due to spin-orbit coupling (SOC), ΔE_s , which is presented in the inset as a function of the crystal momentum.

bital subspace (pseudospin degree of freedom), respectively. The function $d_0(\mathbf{k})$ and the components of the pseudospin vector $\mathbf{d}(\mathbf{k}) = [d_1(\mathbf{k}), d_2(\mathbf{k}), d_3(\mathbf{k})]$ are given by $d_0(\mathbf{k}) = C - Dk^2$, $d_1(\mathbf{k}) = -Ak_y + G(k_x^2 - k_y^2)$, $d_2(\mathbf{k}) = Ak_x - 2Gk_xk_y$, and $d_3(\mathbf{k}) = M - Bk^2$. The spin-up and down blocks $[h(\mathbf{k})]$ and $h^*(-\mathbf{k})$, respectively] are connected by TRS.

To investigate in more detail the topology of Na₂CdSn, we perform a square lattice regularization on Eq. (25), which consists of substituting $k_i \to \sin{(ak_i)}/a$ and $k_i^2 \to 2\left[1-\cos{(ak_i)}\right]/a^2$ (i=x,y) [55]. This substitution is valid for $|k_i| \ll 1/a$ and, therefore, expected to be valid in our region of interest.

Using the parameters in Table III, we show in Fig. 3-a) the spin-up energy bands along the high-symmetry path $Y-\Gamma-X$ for both continuous and regularized models. Here, $\Gamma=(0,0),\ X=(\pi/a,0),\ Y=(0,\pi/a)$ and $M=(\pi/a,\pi/a)$ are high-symmetry points of the first BZ for the square lattice. The energy bands are plotted only within the region of interest, $\sim 3\%$ of the high-symmetry lines, i.e., $0\leq |k|\lesssim 0.09\,a^{-1}$. The black solid and red dashed curves represent the energy bands of the continuous and regularized models, respectively. In Fig. 3-b) we show the spin-up energy bands along 3% of the $M-\Gamma-X$ high-symmetry path, which for the $\Gamma-M$ direction corresponds to $0\leq |k|\lesssim 0.13\,a^{-1}$.

The excellent agreement between the continuous and regularized models around the Γ point is clear from Figs. 3-a) and 3-b). In addition, we have confirmed (by plotting the energy bands along the full path, not shown) that the regularization procedure preserves the overall gap, which is important to calculate an integer-valued topological invariant [55].

The pseudospin unit vector for the regularized model

 $\hat{d}(\mathbf{k}) = d(\mathbf{k})/|d(\mathbf{k})|$ defines a mapping from the compact BZ to the unit Bloch sphere. The number of times this mapping wraps the Bloch sphere defines an integer-quantized topological invariant known as the winding number [55, 85, 86]. In Fig. 3-c), we show the skyrmion configuration obtained for Na₂CdSn. Each vector is defined by the three components of $\hat{d}(\mathbf{k})$ at the corresponding \mathbf{k} point of the BZ, and the color code denotes the $\hat{d}_3(\mathbf{k})$ component. We can see that, at the Γ point, the vector field points in the positive z direction, while at the corners of the BZ, the vectors point in the negative z direction. Additionally, the skyrmion configuration in Fig. 3-c) resembles that of a second-order antiskyrmion, which alludes to a topological charge of -2 [87–90].

To unequivocally identify the topological phase of the regularized model, we calculate the Chern number for the valence bands of each spin sector separately. The first step is to define the Berry connection $\mathbf{A}_v^{\uparrow(\downarrow)}(\mathbf{k}) = -i \langle u_v^{\uparrow(\downarrow)}(\mathbf{k}) | \nabla_{\mathbf{k}} | u_v^{\uparrow(\downarrow)}(\mathbf{k}) \rangle$ and Berry curvature $F_v^{\uparrow(\downarrow)}(\mathbf{k}) = \hat{z} \cdot \left[\nabla_{\mathbf{k}} \times \mathbf{A}_v^{\uparrow(\downarrow)}(\mathbf{k}) \right]$ [55], where $|u_v^{\uparrow(\downarrow)}(\mathbf{k}) \rangle$ denotes the valence band of the corresponding spin sector. Now we define the Chern number for each spin sector using the well-known TKNN formula [91], which consists of integrating the Berry curvature over the whole BZ [55]:

$$C^{\uparrow(\downarrow)} = \frac{1}{2\pi} \int_{BZ} d^2k F_v^{\uparrow(\downarrow)}(\mathbf{k}). \tag{26}$$

Due to TRS, the total Chern number must be zero, i.e., $C = (C^{\uparrow} + C^{\downarrow}) = 0$. By calculating the Chern numbers numerically, we obtain $C^{\uparrow} = -2$ and $C^{\downarrow} = 2$ for our system, consistent with the second-order antiskyrmion configuration in Fig. 3-c). This is related to the presence of the Gk_{\pm}^2 terms in the off-diagonal matrix elements of

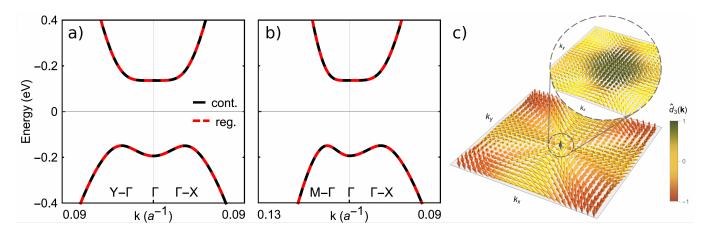


Figure 3. (Color online) Comparison between spin-up energy bands for the continuous (solid black curves) and regularized (dashed red curves) models along 3% of the a) $Y - \Gamma - X$ and b) $M - \Gamma - X$ high-symmetry paths of the square-lattice Brillouin zone (BZ), corresponding to the region of interest. The crystal momentum intervals along each direction are given by $0 \le |k| < 0.09/a$ along either $\Gamma - X$ or $\Gamma - Y$, and $0 \le |k| < 0.03\sqrt{2}\pi/a$ along the $\Gamma - M$ direction. c) Pseudospin skyrmion configuration of the regularized model over the first BZ, i.e., $0 < |k_{x(y)}| < \pi/a$. Each arrow is determined by the components of the pseudospin unit vector at the corresponding \mathbf{k} point, $\hat{\mathbf{d}}(\mathbf{k})$, with the color code given by the $\hat{d}_3(\mathbf{k})$ component. The inset shows a zoom into the region of interest, where we can see in more detail the behavior of the vector field around the Γ point. The ranges for the components of the crystal momentum in the inset are given by $0 < |k_{x(y)}| < 0.02\pi/a$.

the $\mathbf{k} \cdot \mathbf{p}$ Hamiltonian in Eq. (15). For G = 0 (with the remaining parameters unchanged), the Chern numbers are given by $C^{\uparrow} = 1$ and $C^{\downarrow} = -1$.

An important topological invariant used to characterize 2D TIs is the so-called spin Chern number [25–28, 92–95], defined as

$$C_s = \frac{1}{2} \left(C^{\uparrow} - C^{\downarrow} \right). \tag{27}$$

For our system, $C_s = -2$, which characterizes the presence of a TI phase. Note that, at zero temperature, the spin Hall conductivity within the bulk band gap is related to the spin Chern number via $\sigma_s = C_s(e/2\pi)$ [2]. Therefore, we predict that $\sigma_s = -2e/2\pi$ for Na₂CdSn.

We now calculate the mirror Chern number [32], a topological invariant often used to classify TCIs protected by mirror symmetry [19–21, 96]. Since the mirror operator for fermions satisfies $\hat{\sigma}_h^2 = -1$, its eigenvalues are given by $\pm i$ (see Appendix A). Due to the simple diagonal matrix representation of the mirror operator in our model [Eq. (20)], we can readily label spin-up (spin-down) energy bands with the mirror eigenvalue -i (+i). In analogy to the spin Chern number, the mirror Chern number can be defined as [32]

$$C_m = \frac{1}{2} \left(C^{-i} - C^{+i} \right),$$
 (28)

where $C^{\pm i}$ is obtained by substituting $\uparrow(\downarrow) \to +i(-i)$ in Eq. (26). For our system, $C_m = -2$.

As shown above, Na₂CdSn hosts the TI and TCI phases simultaneously; thus, it can be classified as a DTI protected by TRS and mirror symmetry. Note that both topological invariants (spin and mirror Chern numbers)

are equal to -2 (in sharp contrast with the spin and mirror Chern numbers -1 reported in Ref. [70]). According to the bulk-boundary correspondence [23, 24], the Na₂CdSn triatomic layer in a finite geometry must have two pairs of counterpropagating helical edge states at each of its boundaries [85]. We explore this feature in the next section.

Unlike well-known conventional TIs [5, 10], the band inversion in Na₂CdSn does not follow the closure of a trivial bulk band gap. Here, the topological gap arises from the SOC-induced lifting of a zone-centered nodal point [Figs. 1-d) and 1-e)]. The nodal point degeneracy is enforced by the 2D irrep Γ_6 of the low-energy conduction and valence bands. Once SOC is considered, the degeneracy is immediately lifted [Figs. 1-f) and 1-g)], resulting in a topologically nontrivial band gap characterized by the spin and mirror Chern numbers -2.

We note that the topology of Na₂CdSn is fundamentally distinct from reported systems with similar crystal structures, such as Na₂MnPb and α -Bi. The former has been predicted to be a ferromagnetic DTI with $C_s=1$ and broken TRS [97], while the latter is predicted to have $C_s=2$ but no crystal-symmetry-related topological invariant [98]. Additionally, it is noteworthy that Ref. [85] reported a nontrivial spin Chern number $C_s=2$ in a generic model for 2D mirror-symmetric paramagnetic semiconductors. However, the mirror Chern number, proposed in Ref. [32], was not investigated in their study.

V. TOPOLOGICAL EDGE STATES

Let us now investigate the existence of topological edge states predicted by the nontrivial topological invariants calculated in Sec. IV. In Sec. VA, we analytically obtain the edge states for a semi-infinite plane geometry. In Sec. VB, we perform a numerical study of the topological edge states in a ribbon geometry.

A. Semi-infinite plane

We first consider a semi-infinite plane geometry consisting of vacuum and the DTI material occupying the x < 0 and x > 0 half-planes, respectively. Such geometry can be modeled by a piecewise potential given by

$$V(x) = \begin{cases} 0 & x \ge 0, \\ +\infty & x < 0. \end{cases}$$
 (29)

Note that the system is no longer periodic along the x direction, so k_x is not a good quantum number. On the other hand, translation symmetry is preserved along the y direction, so k_y is still a good quantum number. We then employ the envelope function approach and perform the substitution $k_x \to -i\partial_x$ in the $k \cdot p$ model Hamiltonian [99, 100].

In this geometry, any edge-localized eigenstate $\Psi_{k_y}(x,y)$ must satisfy the following boundary conditions:

$$\Psi_{k_n}(x=0,y) = 0 \quad \forall y \in \mathbb{R},\tag{30}$$

$$\lim_{x \to +\infty} \Psi_{k_y}(x, y) = 0 \quad \forall y \in \mathbb{R}, \tag{31}$$

$$\Psi_{k_n}(x, y + L_y) = \Psi_{k_n}(x, y) \quad \forall (x, y) \in \mathbb{R}^2. \tag{32}$$

Equation (32) is the Born-von Karman boundary condition, with L_y the length of the system in the y direction.

Consider the Schrödinger equation for the spin-up block $h(k_x \to -i\partial_x, k_y)\psi(x,y) = E\psi(x,y)$, where h(k) is defined by Eq. (25) and $\psi(x,y)$ is a particular two-component envelope function solution. The wave function $\psi(x,y)$ can be separated into a product of two factors, one corresponding to plane waves along the y direction and the other corresponding to a nonperiodic function along x. This allows us to write the following ansatz [100]

$$\psi_{\kappa_x, k_y}(x, y) = \frac{\exp(ik_y y)}{\sqrt{L_y}} \begin{pmatrix} 1\\ R_{\kappa_x, k_y} \end{pmatrix} \exp(i\kappa_x x), \quad (33)$$

where $\kappa_x(k_y, E)$ represents the transversal modes and R_{κ_x, k_y} is the ratio between the two wave function components. The normalization constant will be introduced later in the general solution.

Substituting Eq. (33) into the Schrödinger equation, we obtain four modes given by $\kappa_x = (-1)^j \kappa_{\pm}$, where $j = \{0, 1\}$ and

$$\kappa_{\pm} \equiv \sqrt{-k_y^2 - F \pm \sqrt{F^2 - Q^2}},\tag{34}$$

with

$$F \equiv \frac{A^2 - 2MB - 2D\bar{E} - 6AGk_y}{2(B^2 + G^2 - D^2)},$$
 (35)

$$Q^2 \equiv \frac{M^2 - \bar{E}^2 + 8AGk_y^3}{(B^2 + G^2 - D^2)},\tag{36}$$

$$\bar{E} \equiv E - C. \tag{37}$$

For each κ_x , R_{κ_x,k_y} is given by

$$R_{k_y\pm}^j = -\frac{iA\left[(-1)^j \kappa_{\pm} + ik_y\right] + G\left[(-1)^j \kappa_{\pm} - ik_y\right]^2}{d_{k_y\pm}},$$
(38)

where $d_{k_y\pm} = -M - \bar{E} + (B - D)(\kappa_{\pm}^2 + k_y^2)$. From now on, we use $R_{k_y\pm}^j \equiv R_{\pm}^j$. Using Eqs. (33), (34), and (38), we write the general solution as the linear combination of the four modes:

$$\Psi_{k_y}(x,y) = \frac{\exp(ik_y y)}{\sqrt{L_y}}$$

$$\times \sum_{\substack{j=0,1\\l=+,-}} c_{j,l} \begin{pmatrix} 1\\R_l^j \end{pmatrix} \exp[i(-1)^j \kappa_l x]. \quad (39)$$

By substituting the fitted parameters into Eq. (34) and plotting the imaginary part of κ_{\pm} , we find $\operatorname{Im}(\kappa_{+}) > 0$, $\forall (k_{y}, E) \in \mathbb{R}^{2}$. On the other hand, $\operatorname{Im}(\kappa_{-})$ can be either positive or negative depending on the values of (k_{y}, E) . For $\operatorname{Im}(\kappa_{-}) > 0$, the general solution, along with the boundary conditions defined in Eqs. (30-32), leads to

$$c_{0,-} = -c_{0,+}, (40)$$

$$c_{1,+} = c_{1,-} = 0, (41)$$

$$R_{\perp}^{0} = R_{-}^{0}. \tag{42}$$

Note that, in applying the boundary conditions in Eqs. (30)-(32), we have already neglected the exponential terms that do not result in square-integrable solutions, i.e., that do not yield a vector Hilbert space. Using Eqs. (39)-(42), we obtain

$$\Psi_{k_y}(x,y) = c_{0,+} \frac{\exp(ik_y y)}{\sqrt{L_y}} \times \left\{ \frac{\exp(i\kappa_+ x) - \exp(i\kappa_- x)}{R_+^0 \left[\exp(i\kappa_+ x) - \exp(i\kappa_- x) \right]} \right\}, \quad (43)$$

where $c_{0,+}$ is determined by normalizing the wave function. Similarly, for $\text{Im}(\kappa_{-}) < 0$, we have

$$c_{1,-} = -c_{0,+}, (44)$$

$$c_{1,+} = c_{0,-} = 0, (45)$$

$$R_{\perp}^{0} = R_{\perp}^{1},$$
 (46)

and

$$\Psi_{k_y}(x,y) = c_{0,+} \frac{\exp(ik_y y)}{\sqrt{L_y}} \times \left\{ \begin{aligned} &\exp(i\kappa_+ x) - \exp(-i\kappa_- x) \\ &R_+^0 \left[\exp(i\kappa_+ x) - \exp(-i\kappa_- x) \right] \end{aligned} \right\}. \quad (47)$$

By solving Eqs. (42) and (46) for E as a function of k_{ν} , we obtain two independent quadratic dispersion relations for the edge states of the spin-up sector. Due to TRS, the two dispersion relations for the edge states with spindown can be readily calculated by replacing $k_u \rightarrow -k_u$ in the solutions for spin-up. We then have

$$E_i^{\uparrow(\downarrow)} = b_{i,0} \pm b_{i,1} k_y + b_{i,2} k_y^2, \quad (i = 1, 2),$$
 (48)

where

$$b_{1(2),0} = C - \frac{DMB \pm |MG|\sqrt{B^2 + G^2 - D^2}}{B^2 + G^2},$$
 (49)

$$b_{1(2),1} = A \frac{-DG \pm B \operatorname{sgn}(MG) \sqrt{B^2 + G^2 - D^2}}{B^2 + G^2}, \quad (50)$$

$$b_{1(2),2} = 2 \frac{-DG^2 \pm |BG| \sqrt{B^2 + G^2 - D^2}}{B^2 + G^2} \quad (51)$$

$$b_{1(2),2} = 2 \frac{-DG^2 \pm |BG|\sqrt{B^2 + G^2 - D^2}}{B^2 + G^2}$$
 (51)

and sgn(x) = +1 (-1) if x > 0 (x < 0).

In Fig. 4, we show the analytical dispersion relations of the spin-up (red curve) and down (blue) edge states [Eq. (48)] for the fitted parameters (Sec. IIIC). The gray-shaded areas represent the continua of delocalized bulk states (bulk region), whose boundaries are indicated by solid black lines.

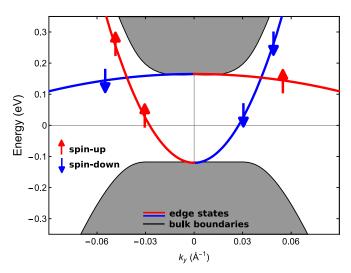


Figure 4. (Color online) Topological edge states hosted by the $\mathbf{k} \cdot \mathbf{p}$ model in a semi-infinite plane geometry, with parameters from the fitting for Na₂CdSn. The red (blue) solid lines represent the analytical solutions for the dispersion relations of the spin-up (down) edge states [Eq. (48)], while the solid black lines delimit the bulk region, corresponding to the continua of delocalized bulk states (gray-shaded areas).

For each energy level inside the bulk band gap, there are two pairs of counterpropagating topological edge states of opposite spin. This is in agreement with the bulk-boundary correspondence theorem, considering the topological invariants calculated in Sec. IV. As it can be seen from Eq. (51), the quadratic dispersion relation of the topological edge states is a consequence of the nonzero parameter G.

Note that all edge states merge into the bulk region at $k_y \approx 0$. As k_y moves away from zero, however, the energy of the edge states increases (in absolute value) slower than the energy of the bulk bands. Hence, here, the edge states never merge into the bulk region again. We emphasize that the effective model derived in Sec. III is only valid in the region close to $k_y = 0$; thus, we should not expect it to capture any realistic merging points that might occur at larger values of k_y . The absence of merging points is also observed when we consider edge states arising from the BHZ Hamiltonian in the absence of k^2 diagonal terms [101].

B. Ribbon geometry

In this section, we apply the finite difference method to obtain the electronic band structure for Na₂CdSn in a ribbon (strip) geometry [102]. We use the parameters in Table III and consider open (periodic) boundary conditions along the x(y) direction.

In Fig. 5-a), we show the electronic band structure for a ribbon of width $W = 100 \,\mathrm{nm}$, i.e., a wide ribbon (compared with the lattice parameter $a = 4.978 \,\text{Å}$). Each (k_u, E) point is colored according to its spin, with red (blue) representing spin-up (down) states. The energy bands forming a Mexican-hat-like structure constitute the bulk region. The energy gap $E_g \approx 285 \,\mathrm{meV}$ between the lowest bulklike conduction and topmost bulklike valence bands is indicated in the figure.

The quadratic energy bands crossing the bulk band gap correspond to the topological edge states. All energy bands are quasidegenerate, including the edge states for which the spin splittings are $\sim 10^{-1}$ meV. Like the spin splitting of the energy bands in the infinite bulk system [Fig. 2-c)], the spin splitting of the edge states is not accompanied by a mixing of the spin components due to the block-diagonal structure of the effective Hamiltonian [Eq. (15)].

The quasidegenerate topological edge states are localized at opposite sides of the strip. Note that, in the wideribbon limit, the energy dispersions of the edge states localized on the left (right) side can be mapped onto those of a vacuum/DTI (DTI/vacuum) semi-infinite system. In analogy to Sec. VA, we employ the envelope function approach and solve the problem for the DTI/vacuum geometry. We use the analytical solutions for the two semiinfinite systems to derive an expression for the inter-edge splitting. Subtracting the dispersion relations for spin-up and spin-down states, we obtained that the spin splittings

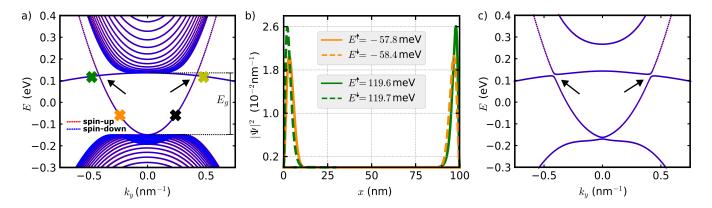


Figure 5. (Color online) Electronic states for Na₂CdSn in a ribbon geometry. a) Electronic band structure showing spin-up (red) and spin-down (blue) states with a small spin splitting caused by the bulk inversion asymmetry (BIA) and k-dependent spin-orbit coupling (SOC). The bulk region is determined by the Mexican-hat-like energy bands, with a bulk band gap of $E_g \approx 285$ meV. The quadratic energy bands correspond to quasidegenerate topological edge states, with the spin split states localized at opposite sides of the ribbon. The colored cross marks indicate the selected edge states for our wave function analysis, and the two black arrows denote the points of edge state crossings. b) Probability densities of the selected topological edge states as functions of x (coordinate along the transversal direction). The color of the curves corresponds to the colors of the respective cross marks, while the solid (dashed) style represents spin-up (spin-down) states. c) Electronic band structure for Na₂CdSn in a ribbon geometry of width W = 15 nm. The black arrows indicate the opening of an anticrossing hybridization gap due to the finite-size effect.

are given by $2b_{1,1}k_y$ and $2b_{2,1}k_y$ for the concave up and down bands, respectively.

Notice that there is no structural inversion asymmetry in this case, which for the BHZ model is known to generate a Rashba term [103–107] that lifts the degeneracy of the topological edge states [107]. For the ribbon geometry considered here, the spin splitting arises solely from the BIA. It can be shown that the inclusion of BIA in the BHZ Hamiltonian [100, 108] also leads to interedge spin splitting in 2D TIs, although in this case, the splitting is accompanied by a mixing of the spin components.

In Fig. 5-b), we present the probability density of the edge states, indicated by the green and orange cross marks in Fig. 5-a), as functions of x (x = 0 and x = W correspond to the ribbon extremities). Each cross mark represents two quasidegenerate states localized at opposite sides of the ribbon (the line colors match the colors of the corresponding cross mark). The dashed (solid) green line corresponds to a spin-down (spin-up) state localized at the left (right) side of the ribbon. Similarly, the solid (dashed) orange line corresponds to a spin-up (spin-down) state localized at the left (right) side of the ribbon. Note that the states shown by the green color are slightly more localized than the ones represented in orange 3 .

So far, we have only investigated the edge states for negative crystal momentum $(k_y \approx -0.24\,\mathrm{nm}^{-1})$ and $k_y \approx -0.48\,\mathrm{nm}^{-1})$. Since our model is invariant under TRS, each topological edge state has a Kramers partner localized on the same side of the ribbon but with opposite momentum and spin. The yellow (black) cross mark in Fig. 5-a) indicates the two Kramers partners of the two states indicated by the green (orange) cross mark. We have verified that, in the wide-ribbon limit, the dispersion relations for the edge states localized at the left side of the ribbon agree exactly with those obtained for the semi-infinite plane geometry [see Eq. (48) and Fig. 4].

The edge states indicated by the green cross mark in Fig. 5-a) have a positive group velocity. Therefore, the spin-up state represented by the green solid curve in Fig. 5-b) propagates on the right edge along the +ydirection, while the spin-down state represented by the green dashed curve propagates on the left edge, also along the +y direction. Their Kramers partners (yellow cross mark), on the other hand, have a negative group velocity, so there is a spin-down state propagating along the -ydirection on the right edge and a spin-up state propagating along the -y direction at the left edge of the ribbon. For the orange cross mark, the edge states have a negative group velocity. Therefore, the states represented by the orange color propagate along the -y direction, while their Kramers partners (black cross mark) propagate along the +y direction.

For any energy level within the bulk band gap (e.g.,

³ A zoom-in on the probability density distributions shown in Fig. 5-b) reveals that the green (orange) curves present a normal (oscillatory) exponential decay with x. The decaying behavior of a given edge state is dictated by the region where it is found in the electronic band structure. This effect is well-discussed for the BHZ model in Ref. [109]. In our model, however, such an anal-

ysis is much more complicated. Therefore, we plan to provide a more detailed investigation of this topic in a forthcoming work.

at the Fermi level), there are four topological edge states at each side of the ribbon. On the left side, there are two spin-down (up) edge states propagating along the +y (-y) direction, while on the right side, there are two spin-up (down) edge states propagating along the +y (-y) direction.

The black arrows in Fig. 5-a) point to the two edge state crossings taking place around the same energy level $E \approx 0.123 \,\mathrm{eV}$. At each crossing point, there are four topological edge states. Let us focus on the edge state crossing around $k_y \approx -0.4~{\rm nm}^{-1}$ (left black arrow). Two of the four edge states live on the same side of the strip, have opposite spins, and propagate along opposite directions. Since they live in different spin subspaces, they are orthogonal to each other and do not hybridize. The counterpropagating states localized at opposite sides of the ribbon, on the other hand, belong to the same spin subspace, and therefore, can hybridize. Naturally, the hybridization requires a superposition of their wave functions, the so-called finite-size effect [109, 110]. In Fig. 5-c), we show the electronic band structure for Na₂CdSn in a ribbon of width $W = 15 \,\mathrm{nm}$. For this narrow ribbon, the edge states (with the same spin) living on opposite sides of the strip hybridize. The hybridization gap due to the anti-crossing of the edge state bands around $k_y \approx -0.4 \, \mathrm{nm}^{-1}$ and $k_y \approx 0.4 \, \mathrm{nm}^{-1}$ are indicated by the two black arrows in the figure.

VI. CONCLUSIONS

We have obtained the electronic band structure of the quasi-2D ternary Na_2CdSn triatomic layer via DFT calculations and derived an effective 4×4 model using the $k \cdot p$ method to describe the low-energy states. To do so, we have employed the Lödwin perturbation theory, the folding-down technique, and the theory of invariants. Our rigorously derived effective Hamiltonian contrasts with that of Ref. [70]. It has some quadratic off-diagonal terms (absent in Ref. [70]) that are crucial to obtain our spin and mirror Chern numbers and the corresponding (two pairs of) protected edge states.

More specifically, by fitting our effective model to the DFT energy bands, we have obtained numerical values for the model parameters and predicted that Na₂CdSn is a DTI with spin and mirror Chern numbers given by $C_s = -2$ and $C_m = -2$, respectively. Using the envelope function approach, we have also obtained analytical dispersion relations, quadratic in the crystal momentum, for the topological edge states in the semi-infinite plane geometry. The edge modes have also been analyzed numerically in the ribbon geometry. For both geometries, we have found two pairs of counterpropagating topological edge states at each boundary, as expected from the bulk-boundary correspondence. Both our Chern numbers and the corresponding (number of) edge states are in blatant contrast with the results in Ref. [70]; there, spin and mirror Chern numbers -1 were reported and,

consequently, only one pair of topological edge states.

Our investigation contributes to the understanding of Na_2CdSn as a giant gap $(E_q = 234.8 \,\mathrm{meV})$ DTI in 2D by providing its proper model Hamiltonian and the corresponding effective $\mathbf{k} \cdot \mathbf{p}$ parameters. This enables us to derive the energy dispersions and wave functions of the edge states arising in finite geometries of this material. The Na_2XY (X = Mg, Cd; Y = Pb, Sn) family of triatomic layers are the building stacking blocks of 3D van der Waals Dirac semimetals, already synthesized experimentally [45, 46]. They can also be potentially obtained via mechanical exfoliation. The DTI Na₂CdSn represents a promising alternative to conventional small-gap TIs in 2D – which usually require the engineering of elaborated quantum wells [5, 6, 58, 103, 111]. We are optimistic that our findings will stimulate the experimental verification of the DTI phase in this outstanding candidate for realistic room-temperature applications in nanotechnology, such as nanoelectronic, spintronic, thermoelectric, and optical devices. As more specific possibilities, we envisage the implementation of Na₂CdSn in topological transistors [42, 112] and topological quantum point contacts [60] for increased device robustness.

VII. ACKNOWLEDGMENTS

W.H.C. acknowledges helpful discussions with Michael Flatté and Jaroslav Fabian. This paper was supported by the National Council for Scientific and Technological Development (CNPq) Grant No. 301595/2022-4, PDJ Process No. 152321/2020-9, and Grant No. 306122/2018-9; by Coordenação de Aperfeiçoamento de Pessoal de Nível Superior (PNPD/CAPES); by São Paulo Research Foundation (FAPESP), Grant No. 2020/00841-9. J.Z. acknowledges the financial support of the Quantimony (Marie Sklodowska-Curie Project Grant No. 956548). P.E.F.J and W.H.C. acknowledge the financial support of the Deutsche Forschungsgemeinschaft (DFG, German Research Foundation) SFB 1277 (Project-ID No. 314695032, Projects No. B07 and No. B11). P.E.F.J. acknowledges the financial support of the DFG-SPP 2244 (Project No. 443416183). W.H.C. acknowledges funding from the Deutsche Forschungsgemeinschaft (DFG) Grant No. TRR 173 268565370 (Project A03).

Appendix A: Mirror symmetry operation

To properly define the mirror symmetry operation about the z axis (in this case, the mirror plane is the xy plane), we consider its effect on both spin and spatial degrees of freedom since spinful electrons live in the state space given by the direct product between the spin and orbital subspaces [113, 114]. The spin angular momentum transforms as an axial vector, and therefore, the components of the spin operator perpendicular and par-

allel to the mirror plane must satisfy, respectively,

$$\left[\hat{\sigma}_h, \hat{S}_z\right] = 0 \quad \text{and} \quad \left\{\hat{\sigma}_h, \hat{S}_i\right\} = 0,$$
 (A1)

with i = x, y [115]. The mirror symmetry operator, consistent with Eq. (A1), is given by the direct product:

$$\hat{\sigma}_h = \hat{\sigma}_h^{spin} \otimes \hat{\sigma}_h^{orb},\tag{A2}$$

where $\hat{\sigma}_h^{spin}$ and $\hat{\sigma}_h^{orb}$ are the mirror symmetry operators in the spin and orbital vector subspaces, respectively.

The $\hat{\sigma}_h^{spin}$ operator can be defined as a π rotation about the z axis followed by the inversion operation (both in the spin subspace) [20, 32, 116], that is,

$$\hat{\sigma}_h^{spin} = \hat{I}^{spin} \hat{R}_z^{spin}(\pi). \tag{A3}$$

The inversion operator does not affect spin degrees of freedom, and therefore, it corresponds to the identity operator in the spin subspace [32]. As usual, the rotation operator is given by [114]

$$\hat{R}_z^{spin}(\pi) = \exp\left(-i\frac{\hat{S}_z}{\hbar}\pi\right) = -i\hat{\sigma}_z,$$
 (A4)

where we have used $\hat{S}_z = \frac{\hbar}{2}\hat{\sigma}_z$. Hence, the mirror operator in the state space [Eq. (A2)] reads

$$\hat{\sigma}_h = -i\hat{\sigma}_z \otimes \hat{\sigma}_h^{orb}.\tag{A5}$$

Applying the $\hat{\sigma}_h^{orb}$ operator twice returns the spatial functions to their original state, so that $(\hat{\sigma}_h^{orb})^2 = 1$.

However, when spin is considered, applying the mirror operation twice leads to a change of sign

$$\hat{\sigma}_h^2 = -1,\tag{A6}$$

which yields the eigenvalues of $\hat{\sigma}_h$ being i and -i [20, 32].

To obtain the matrix representation of $\hat{\sigma}_h$, we can use Eq. (A5), and project $\hat{\sigma}_z$ and $\hat{\sigma}_h^{orb}$ onto the basis of the spin and orbital subspaces, respectively. The basis functions for the orbital subspace are determined by the irreps of the simple group relevant for the material under consideration.

The mirror symmetry has important consequences for the spin texture of the energy bands. Let $|\psi_{\boldsymbol{k},\eta}\rangle$ be a Bloch state with mirror eigenvalue η . Taking the expectation values of the spin components gives

$$\langle \hat{S}_z \rangle = \langle \psi_{\mathbf{k},\eta} | \hat{\sigma}_h^{-1} \hat{\sigma}_h \hat{S}_z \hat{\sigma}_h^{-1} \hat{\sigma}_h | \psi_{\mathbf{k},\eta} \rangle$$
$$= |\eta|^2 \langle \hat{S}_z \rangle = \langle \hat{S}_z \rangle$$
 (A7)

and

$$\begin{split} \left\langle \hat{S}_{i} \right\rangle &= \left\langle \psi_{\boldsymbol{k},\eta} \middle| \hat{\sigma}_{h}^{-1} \hat{\sigma}_{h} \hat{S}_{i} \hat{\sigma}_{h}^{-1} \hat{\sigma}_{h} \middle| \psi_{\boldsymbol{k},\eta} \right\rangle = -|\eta|^{2} \left\langle \hat{S}_{i} \right\rangle \\ &= -\left\langle \hat{S}_{i} \right\rangle = 0 \quad (i=x,y), \\ \text{where we have used Eq. (A1). Therefore, for the } |\psi_{\boldsymbol{k},\eta} \rangle \end{split}$$

where we have used Eq. (A1). Therefore, for the $|\psi_{\mathbf{k},\eta}\rangle$ Bloch state the spin texture must be polarized along the z direction in the whole BZ, except at degeneracies [54].

Appendix B: Expressions for the model parameters in the Löwdin perturbation approach

In Sec. III A, we have shown the effective $k \cdot p$ Hamiltonian derived using the Löwdin perturbation theory. Below, we show the explicit expressions for the parameters of the model. The parameters A_1 and A_2 are given, respectively, by

$$A_1 = \left(\frac{\hbar}{m_0}\right)^2 \left[\sum_{\beta}^{B[\Gamma_1]} \frac{|\langle X|p_x|\Gamma_{1\beta}\rangle|^2}{\epsilon_0 - E_{\Gamma_{1\beta}}} + \sum_{\beta}^{B[\Gamma_6]} \frac{|\langle X|p_x|\Gamma_{6\beta}^x\rangle|^2}{\epsilon_0 - E_{\Gamma_{6\beta}}}\right],\tag{B1}$$

and

$$A_2 = \left(\frac{\hbar}{m_0}\right)^2 \left[\sum_{\beta}^{B[\Gamma_2]} \frac{|\langle X|p_y|\Gamma_{2\beta}\rangle|^2}{\epsilon_0 - E_{\Gamma_{2\beta}}} + \sum_{\beta}^{B[\Gamma_6]} \frac{|\langle X|p_x|\Gamma_{6\beta}^x\rangle|^2}{\epsilon_0 - E_{\Gamma_{6\beta}}}\right],\tag{B2}$$

where we have used $\langle X|p_y|\Gamma_{6\beta}^y\rangle = -\langle X|p_x|\Gamma_{6\beta}^x\rangle$ (similar relations were used to simplify all the matrix elements below). In the expressions above, $B[\Gamma_i]$ indicates that β

runs over all infinite remote bands belonging to the Γ_i irrep. When the irrep of the β th band is 1D, its single basis function is written as $|\Gamma_{i\beta}\rangle$. For irreps of higher

dimensions, we use $|\Gamma_{i\beta}^{\mu}\rangle$ to denote the basis function that transforms according to μ , i.e., $|\Gamma_{i\beta}^{\mu}\rangle \sim \mu$, ($\mu = x, y, R_x, R_y$...). Here, $E_{\Gamma_{i\beta}}$ is the energy of the β th band belonging to the Γ_i irrep. Naturally, all basis functions of

an irrep have the same energy eigenvalue, and therefore, it is not necessary to label the energy eigenvalue with the basis function. The remaining parameters read

$$D_1 = -\frac{\hbar^2}{4m_0^3 c^2} \left[2 \sum_{\beta}^{B[\Gamma_6]} \frac{\langle X | p_x | \Gamma_{6\beta}^x \rangle \langle \Gamma_{6\beta}^y | A_z | X \rangle}{\epsilon_0 - E_{\Gamma_{6\beta}}} \right], \tag{B3}$$

$$B = -i\frac{\hbar^3}{4m_0^3c^2} \left[\sum_{\beta}^{B[\Gamma_1]} \frac{\langle X|p_x|\Gamma_{1\beta}\rangle\langle\Gamma_{1\beta}|\partial_xV|X\rangle}{\epsilon_0 - E_{\Gamma_{1\beta}}} + \sum_{\beta}^{B[\Gamma_2]} \frac{\langle X|p_y|\Gamma_{2\beta}\rangle\langle\Gamma_{2\beta}|\partial_yV|X\rangle}{\epsilon_0 - E_{\Gamma_{2\beta}}} - 2\sum_{\beta}^{B[\Gamma_6]} \frac{\langle X|p_x|\Gamma_{6\beta}^x\rangle\langle\Gamma_{6\beta}^x|\partial_xV|X\rangle}{\epsilon_0 - E_{\Gamma_{6\beta}}} \right], \tag{B4}$$

$$C_{1} = \left(\frac{\hbar}{4m_{0}^{2}c^{2}}\right)^{2} \left[\sum_{\beta}^{B[\Gamma_{6}]} \frac{|\langle X|A_{z}|\Gamma_{6\beta}^{y}\rangle|^{2}}{\epsilon_{0} - E_{\Gamma_{6\beta}}} + \sum_{\beta}^{B[\Gamma_{3}]} \frac{|\langle X|A_{x}|\Gamma_{3\beta}\rangle|^{2}}{\epsilon_{0} - E_{\Gamma_{3\beta}}} + \sum_{\beta}^{B[\Gamma_{4}]} \frac{|\langle X|A_{y}|\Gamma_{4\beta}\rangle|^{2}}{\epsilon_{0} - E_{\Gamma_{4\beta}}} + 2\sum_{\beta}^{B[\Gamma_{5}]} \frac{|\langle X|A_{x}|\Gamma_{5\beta}^{R_{x}}\rangle|^{2}}{\epsilon_{0} - E_{\Gamma_{5\beta}}}\right], \quad (B5)$$

$$C_{2} = \left(\frac{\hbar}{4m_{0}^{2}c^{2}}\right)^{2} \left[\sum_{\beta}^{B[\Gamma_{3}]} \frac{|\langle X|A_{x}|\Gamma_{3\beta}\rangle|^{2}}{\epsilon_{0} - E_{\Gamma_{3\beta}}} + \sum_{\beta}^{B[\Gamma_{4}]} \frac{|\langle X|A_{y}|\Gamma_{4\beta}\rangle|^{2}}{\epsilon_{0} - E_{\Gamma_{4\beta}}} - 2\sum_{\beta}^{B[\Gamma_{5}]} \frac{|\langle X|A_{x}|\Gamma_{5\beta}^{R_{x}}\rangle|^{2}}{\epsilon_{0} - E_{\Gamma_{5\beta}}}\right], \tag{B6}$$

$$E_1 = -i\frac{\hbar^3}{(4m_0^2c^2)^2} \left[2\sum_{\beta}^{B[\Gamma_5]} \frac{\langle X|A_x|\Gamma_{5\beta}^{R_x}\rangle\langle\Gamma_{5\beta}^{R_y}|\partial_z V|X\rangle}{\epsilon_0 - E_{\Gamma_{5\beta}}} \right],\tag{B7}$$

$$F_{1} = \left(\frac{\hbar^{2}}{4m_{0}^{2}c^{2}}\right)^{2} \left[\sum_{\beta}^{B[\Gamma'_{2}]} \frac{|\langle X|\partial_{y}V|\Gamma_{2\beta}\rangle|^{2}}{\epsilon_{0} - E_{\Gamma_{2\beta}}} + \sum_{\beta}^{B[\Gamma_{6}]} \frac{|\langle X|\partial_{x}V|\Gamma_{6\beta}^{x}\rangle|^{2}}{\epsilon_{0} - E_{\Gamma_{6\beta}}} + \sum_{\beta}^{B[\Gamma_{5}]} \frac{|\langle X|\partial_{z}V|\Gamma_{5\beta}^{R_{y}}\rangle|^{2}}{\epsilon_{0} - E_{\Gamma_{5\beta}}} \right], \tag{B8}$$

and

$$F_2 = \left(\frac{\hbar^2}{4m_0^2c^2}\right)^2 \left[\sum_{\beta}^{B[\Gamma_1]} \frac{|\langle X|\partial_x V|\Gamma_{1\beta}\rangle|^2}{\epsilon_0 - E_{\Gamma_{1\beta}}} + \sum_{\beta}^{B[\Gamma_6]} \frac{|\langle X|\partial_x V|\Gamma_{6\beta}^x\rangle|^2}{\epsilon_0 - E_{\Gamma_{6\beta}}} + \sum_{\beta}^{B[\Gamma_5]} \frac{|\langle X|\partial_z V|\Gamma_{5\beta}^{R_y}\rangle|^2}{\epsilon_0 - E_{\Gamma_{5\beta}}} \right]. \tag{B9}$$

Appendix C: Model derivation via the Theory of Invariants

As discussed in the main text, we have also derived the 4×4 effective model in Eqs (8)–(14) by using the theory of invariants [49, 53]. This approach allows one to obtain a finite-dimensional ${\pmb k}\cdot {\pmb p}$ Hamiltonian $H({\pmb k})$ based only on the symmetries of the crystal under consideration. More specifically, it consists of writing $H({\pmb k})$ as a Taylor expansion in the momentum ${\pmb k}$,

$$H(\mathbf{k}) = \sum_{l,m,n} h_{l,m,n} k_x^l k_y^m k_z^n, \tag{C1}$$

and finding the unknown coefficients $h_{l,m,n}$ (matrices) by imposing that the Hamiltonian \mathcal{H} of the crystal, charac-

terized by a point group G, be invariant under all symmetry operations g_i ($g_i \in G$), i.e., $[\mathcal{H}, g_i] = 0$. For the Bloch Hamiltonian $\mathcal{H}(\mathbf{k}) = \exp(-i\mathbf{k}\cdot\mathbf{r})\mathcal{H}\exp(i\mathbf{k}\cdot\mathbf{r})$, this commutator yields

$$\mathcal{H}(u_{q_i}\mathbf{k}) = g_i \mathcal{H}(\mathbf{k}) g_i^{-1}, \tag{C2}$$

where u_{g_i} is the matrix representation of g_i in k space. An equivalent expression can be derived for the projected Hamiltonian H(k) in Eq. (C1), given by

$$H(u_{g_i}\mathbf{k}) = U_{g_i}H(\mathbf{k})U_{g_i}^{-1},\tag{C3}$$

with U_{g_i} the matrix representation of g_i in the Hilbert space. Hence, by using Eq. (C1) and the constraints imposed by Eq. (C3), we obtain a system of equations for

the coefficients $h_{l,m,n}$. Note that, for 2D systems, which is the case we are interested in here, we can simply drop k_z and the sum over n in Eq. (C1).

The Na₂CdSn triatomic layer we are interested in belongs to the point group D_{3h} . To determine $h_{l,m,n}$, it is sufficient to use in Eq. (C3) only the corresponding group generators $\{g_i\} = \{C_{3z}, C_{2x}, \sigma_h\}$, with C_{3z} representing a rotation about the z axis, C_{2x} a rotation about the x axis, and σ_h a mirror plane reflection about the xy plane (see character table in the SM [75]). In addition, we consider that the system is time-reversal symmetric.

Here, we use the QSYMM Python package [117], which receives as input the matrix representations U_{g_i} and g_i , for all $g_i \in G$ (generators + TRS), and returns the matrices $h_{l,m,n}$. The matrix representations U_{g_i} of the generators $\{C_{3z}, C_{2x}, \sigma_h\}$ and time-reversal operator \mathcal{T} follow from both the 2D irrep of the orbital part (Γ_6) and the spinorial part (Γ_7) , i.e., $\Gamma_6 \otimes \Gamma_7 = \Gamma_8 \oplus \Gamma_9$, and are given

$$U_{C_{3z}} = \exp\left(-\frac{i\phi\sigma_3}{2}\right) \otimes \exp(-i\phi\tau_2),$$
 (C4)

$$U_{C_{2x}} = -i\sigma_1 \otimes \tau_3, \tag{C5}$$

$$U_{\sigma_h} = -i\sigma_3 \otimes \tau_0,$$

$$T = -i\sigma_2 \otimes \tau_0 K,$$
(C6)
(C7)

$$T = -i\sigma_2 \otimes \tau_0 K, \tag{C7}$$

with $\phi = 2\pi/3$. Up to second order in the crystal momentum k, the 4×4 Hamiltonian is given by

$$H(\mathbf{k}) = \begin{pmatrix} c_0 & ic_1 & 0 & 0 \\ -ic_1 & c_0 & 0 & 0 \\ 0 & 0 & c_0 & -ic_1 \\ 0 & 0 & ic_1 & c_0 \end{pmatrix} + \begin{pmatrix} c_3k_y & c_3k_x & 0 & 0 \\ c_3k_x & -c_3k_y & 0 & 0 \\ 0 & 0 & -c_3k_y & -c_3k_x \\ 0 & 0 & -c_3k_x & c_3k_y \end{pmatrix}$$

$$+ \begin{pmatrix} c_4k_y^2 + c_5k_x^2 & (c_5 - c_4)k_xk_y + ic_6k^2 & 0 & 0 \\ (c_5 - c_4)k_xk_y - ic_6k^2 & c_4k_x^2 + c_5k_x^2 & 0 & 0 \\ 0 & 0 & c_4k_y^2 + c_5k_x^2 & (c_5 - c_4)k_xk_y - ic_6k^2 \\ 0 & 0 & (c_5 - c_4)k_xk_y + ic_6k^2 & c_4k_x^2 + c_5k_y^2 \end{pmatrix}, \quad (C8)$$

with $k^2 = k_x^2 + k_y^2$.

Equation (C8) is the most general form of the Hamiltonian $H(\mathbf{k})$ allowed by symmetry for our 2D system. A detailed investigation using the results in Sec. III (see also the SM [75]) yields

$$c_0 = \epsilon_0 + C_1, \tag{C9}$$

$$c_1 = -\alpha - C_2,$$
 (C10)
 $c_3 = \zeta + D_1 + E_1,$ (C11)

$$c_3 = \zeta + D_1 + E_1,$$
 (C11)

$$c_4 = A_2 + F_2, \tag{C12}$$

$$c_5 = A_1 + F_1,$$
 (C13)

$$c_6 = -B. (C14)$$

^[1] C. L. Kane and E. J. Mele, Z₂ Topological Order and the Quantum Spin Hall Effect, Phys. Rev. Lett. 95, 146802 (2005).

^[2] C. L. Kane and E. J. Mele, Quantum Spin Hall Effect in Graphene, Phys. Rev. Lett. $\boldsymbol{95},\,226801$ (2005).

^[3] L. Fu and C. L. Kane, Time reversal polarization and a \mathbb{Z}_2 adiabatic spin pump, Phys. Rev. B 74, 195312

^[4] B. A. Bernevig and S.-C. Zhang, Quantum Spin Hall Effect, Phys. Rev. Lett. 96, 106802 (2006).

B. A. Bernevig, T. L. Hughes, and S.-C. Zhang, Quantum Spin Hall Effect and Topological Phase Transition in HgTe Quantum Wells, Science 314, 1757 (2006).

^[6] M. König, S. Wiedmann, C. Brüne, A. Roth, H. Buhmann, L. W. Molenkamp, X.-L. Qi, and S.-C. Zhang, Quantum Spin Hall Insulator State in HgTe Quantum Wells, Science **318**, 766 (2007).

^[7] L. Fu, C. L. Kane, and E. J. Mele, Topological Insulators in Three Dimensions, Phys. Rev. Lett. 98, 106803 (2007).

^[8] L. Fu and C. L. Kane, Topological insulators with inversion symmetry, Phys. Rev. B 76, 045302 (2007).

X.-L. Qi, T. L. Hughes, and S.-C. Zhang, Topological field theory of time-reversal invariant insulators, Phys. Rev. B 78, 195424 (2008).

^[10] H. Zhang, C. X. Liu, X. L. Qi, X. Dai, Z. Fang, and S.-

- C. Zhang, Topological insulators in Bi_2Se_3 , Bi_2Te_3 and Sb_2Te_3 with a single Dirac cone on the surface, Nat. Phys. 5, 438 (2009).
- [11] C.-X. Liu, X.-L. Qi, H. J. Zhang, X. Dai, Z. Fang, and S.-C. Zhang, Model Hamiltonian for topological insulators, Phys. Rev. B 82, 045122 (2010).
- [12] T. L. Hughes, E. Prodan, and B. A. Bernevig, Inversionsymmetric topological insulators, Phys. Rev. B 83, 245132 (2011).
- [13] M. Z. Hasan and C. L. Kane, Colloquium: Topological insulators, Rev. Mod. Phys. 82, 3045 (2010).
- [14] X. L. Qi and S. C. Zhang, Topological insulators and superconductors, Rev. Mod. Phys. 83, 1057 (2011).
- [15] W. H. Campos, W. A. Moura-Melo, and J. M. Fonseca, Geometrically induced reversion of Hall current in a topological insulator cavity, Phys. Lett. A 381, 417 (2017).
- [16] W. Han, Y. Otani, and S. Maekawa, Quantum materials for spin and charge conversion, npj Quantum Mater. 3, 1 (2018).
- [17] W. H. Campos, J. M. Fonseca, V. E. De Carvalho, J. B. Mendes, M. S. Rocha, and W. A. Moura-Melo, Topological Insulator Particles As Optically Induced Oscillators: Toward Dynamical Force Measurements and Optical Rheology, ACS Photonics 5, 741 (2018).
- [18] L. Fu, Topological Crystalline Insulators, Phys. Rev. Lett. 106, 106802 (2011).
- [19] J. Liu, T. H. Hsieh, P. Wei, W. Duan, J. Moodera, and L. Fu, Spin-filtered edge states with an electrically tunable gap in a two-dimensional topological crystalline insulator, Nat. Mater. 13, 178 (2014).
- [20] Y. Ando and L. Fu, Topological Crystalline Insulators and Topological Superconductors: From Concepts to Materials, Annu. Rev. Condens. Matter Phys. 6, 361 (2015).
- [21] C. H. Hsu, Z. Q. Huang, C. P. Crisostomo, L. Z. Yao, F. C. Chuang, Y. T. Liu, B. Wang, C. H. Hsu, C. C. Lee, H. Lin, and A. Bansil, Two-dimensional Topological Crystalline Insulator Phase in Sb/Bi Planar Honeycomb with Tunable Dirac Gap, Sci. Rep. 6, 18993 (2016).
- [22] C. H. Hsu, X. Zhou, T. R. Chang, Q. Ma, N. Gedik, A. Bansil, S. Y. Xu, H. Lin, and L. Fu, Topology on a new facet of bismuth, Proc. Natl. Acad. Sci. U. S. A. 116, 13255 (2019).
- [23] X.-L. Qi, Y.-S. Wu, and S.-C. Zhang, General theorem relating the bulk topological number to edge states in two-dimensional insulators, Phys. Rev. B 74, 045125 (2006).
- [24] R. S. K. Mong and V. Shivamoggi, Edge states and the bulk-boundary correspondence in Dirac Hamiltonians, Phys. Rev. B 83, 125109 (2011).
- [25] L. Sheng, D. N. Sheng, C. S. Ting, and F. D. M. Haldane, Nondissipative spin hall effect via quantized edge transport, Phys. Rev. Lett. 95, 136602 (2005).
- [26] D. N. Sheng, Z. Y. Weng, L. Sheng, and F. D. M. Haldane, Quantum Spin-Hall Effect and Topologically Invariant Chern Numbers, Phys. Rev. Lett. 97, 036808 (2006).
- [27] T. Fukui and Y. Hatsugai, Topological aspects of the quantum spin-Hall effect in graphene: Z₂ topological order and spin Chern number, Phys. Rev. B 75, 121403(R) (2007).
- [28] E. Prodan, Robustness of the spin-Chern number, Phys.

- Rev. B 80, 125327 (2009).
- [29] T. H. Hsieh, H. Lin, J. Liu, W. Duan, A. Bansil, and L. Fu, Topological crystalline insulators in the SnTe material class, Nat. Commun. 3, 982 (2012).
- [30] X. Liu, H.-C. Hsu, and C.-X. Liu, In-Plane Magnetization-Induced Quantum Anomalous Hall Effect, Phys. Rev. Lett. 111, 086802 (2013).
- [31] X. Zhou, C.-H. Hsu, T.-R. Chang, H.-J. Tien, Q. Ma, P. Jarillo-Herrero, N. Gedik, A. Bansil, V. M. Pereira, S.-Y. Xu, H. Lin, and L. Fu, Topological crystalline insulator states in the Ca₂As family, Phys. Rev. B 98, 241104(R) (2018).
- [32] J. C. Y. Teo, L. Fu, and C. L. Kane, Surface states and topological invariants in three-dimensional topological insulators: Application to Bi_{1-x}Sb_x, Phys. Rev. B 78, 045426 (2008).
- [33] I. Matsuda, K. Yaji, A. A. Taskin, M. D'angelo, R. Yukawa, Y. Ohtsubo, P. Le Fèvre, F. Bertran, S. Yoshizawa, A. Taleb-Ibrahimi, A. Kakizaki, Y. Ando, and F. Komori, Surface state of the dual topological insulator Bi₀.91Sb₀.09(112), Phys. B 516, 100 (2017).
- [34] T. Rauch, M. Flieger, J. Henk, I. Mertig, and A. Ernst, Dual Topological Character of Chalcogenides: Theory for Bi₂Te₃, Phys. Rev. Lett. 112, 016802 (2014).
- [35] M. Eschbach, M. Lanius, C. Niu, E. Młyńczak, P. Gospodarič, J. Kellner, P. Schüffelgen, M. Gehlmann, S. Döring, E. Neumann, M. Luysberg, G. Mussler, L. Plucinski, M. Morgenstern, D. Grützmacher, G. Bihlmayer, S. Blügel, and C. M. Schneider, Bi₁Te₁ is a dual topological insulator, Nat. Commun. 8, 14976 (2017).
- [36] H. Lee, Y. G. Kang, M. C. Jung, M. J. Han, and K. J. Chang, Robust dual topological insulator phase in NaZnBi, NPG Asia Mater. 14, 36 (2022).
- [37] J. I. Facio, S. K. Das, Y. Zhang, K. Koepernik, J. van den Brink, and I. C. Fulga, Dual topology in jacutingaite Pt₂HgSe₃, Phys. Rev. Mater. 3, 074202 (2019).
- [38] B. Ghosh, S. Mardanya, B. Singh, X. Zhou, B. Wang, T.-R. Chang, C. Su, H. Lin, A. Agarwal, and A. Bansil, Saddle-point Van Hove singularity and dual topological state in Pt₂HgSe₃, Phys. Rev. B 100, 235101 (2019).
- [39] A. Marrazzo, N. Marzari, and M. Gibertini, Emergent dual topology in the three-dimensional Kane-Mele Pt₂HgSe₃, Phys. Rev. Res. 2, 012063(R) (2020).
- [40] S. Li, W. Ji, J. Zhang, Y. Wang, C. Zhang, and S. Yan, Two-dimensional rectangular bismuth bilayer: A novel dual topological insulator, Front. Phys. 18, 43301 (2023).
- [41] C. Niu, P. M. Buhl, G. Bihlmayer, D. Wortmann, Y. Dai, S. Blügel, and Y. Mokrousov, Robust dual topological character with spin-valley polarization in a monolayer of the Dirac semimetal Na₃Bi, Phys. Rev. B 95, 075404 (2017).
- [42] C. M. Acosta and A. Fazzio, Spin-Polarization Control Driven by a Rashba-Type Effect Breaking the Mirror Symmetry in Two-Dimensional Dual Topological Insulators, Phys. Rev. Lett. 122, 036401 (2019).
- [43] B. Focassio, G. R. Schleder, A. Pezo, M. Costa, and A. Fazzio, Dual topological insulator device with disorder robustness, Phys. Rev. B 102, 045414 (2020).
- [44] W. Li, P. Zhou, and L. Sun, Two-dimensional dual topological insulator in hexagonal IrO, New J. Phys. 25, 023010 (2023).

- [45] B. Peng, C. Yue, H. Zhang, Z. Fang, and H. Weng, Predicting Dirac semimetals based on sodium ternary compounds, npj Comput. Mater. 4, 68 (2018).
- [46] R. Matthes and H.-U. Schuster, Ternäre Natriumphasen mit Cadmium bzw. Quecksilber und Zinn bzw. Blei / Ternary Sodium Phases with Cadmium or Mercury and Tin or Lead, Zeitschrift für Naturforsch. B 35, 778 (1980).
- [47] T. Yamada, T. Ikeda, R. P. Stoffel, V. L. Deringer, R. Dronskowski, and H. Yamane, Synthesis, Crystal Structure, and High-Temperature Phase Transition of the Novel Plumbide Na₂MgPb, Inorg. Chem. 53, 5253 (2014).
- [48] P. O. Löwdin, A note on the quantum-mechanical perturbation theory, J. Chem. Phys. 19, 1396 (1951).
- [49] R. Winkler, Spin-Orbit Coupling Effects in Two-Dimensional Electron and Hole Systems, Vol. 191 (Springer, 2003) p. 228.
- [50] E. Bernardes, J. Schliemann, M. Lee, J. C. Egues, and D. Loss, Spin-orbit interaction in symmetric wells with two subbands, Phys. Rev. Lett. 99, 076603 (2007).
- [51] R. S. Calsaverini, E. Bernardes, J. C. Egues, and D. Loss, Intersubband-induced spin-orbit interaction in quantum wells, Phys. Rev. B 78, 155313 (2008).
- [52] J. Fu, P. H. Penteado, D. R. Candido, G. J. Ferreira, D. P. Pires, E. Bernardes, and J. C. Egues, Spin-orbit coupling in wurtzite heterostructures, Phys. Rev. B 101, 134416 (2020).
- [53] G. L. Bir and G. E. Pikus, Symmetry and Strain-Induced Effects in Semiconductors (John Wiley and Sons, New York, 1974).
- [54] M. Kurpas, P. E. Faria Junior, M. Gmitra, and J. Fabian, Spin-orbit coupling in elemental twodimensional materials, Phys. Rev. B 100, 125422 (2019).
- [55] B. A. Bernevig, Topological Insulators and Topological Superconductors (Princeton University Press, Princeton, 2013) p. 260.
- [56] I. Knez, R. R. Du, and G. Sullivan, Evidence for Helical Edge Modes in Inverted InAs/GaSb Quantum Wells, Phys. Rev. Lett. 107, 136603 (2011).
- [57] I. Knez and R. R. Du, Quantum spin Hall effect in inverted InAs/GaSb quantum wells, Front. Phys. 7, 200 (2012).
- [58] D. R. Candido, M. E. Flatté, and J. C. Egues, Blurring the Boundaries between Topological and Nontopological Phenomena in Dots, Phys. Rev. Lett. 121, 256804 (2018).
- [59] Q.-K. Xue, A topological twist for transistors, Nature nanotechnology 6, 197 (2011).
- [60] J. Strunz, J. Wiedenmann, C. Fleckenstein, L. Lunczer, W. Beugeling, V. L. Müller, P. Shekhar, N. T. Ziani, S. Shamim, J. Kleinlein, et al., Interacting topological edge channels, Nature Physics 16, 83 (2020).
- [61] W. Cao, H. Bu, M. Vinet, M. Cao, S. Takagi, S. Hwang, T. Ghani, and K. Banerjee, The future transistors, Nature 620, 501 (2023).
- [62] D. Awschalom and N. Samarth, Spintronics without magnetism, Physics 2, 50 (2009).
- [63] D. Pesin and A. H. MacDonald, Spintronics and pseudospintronics in graphene and topological insulators, Nature materials 11, 409 (2012).
- [64] A. Mellnik, J. Lee, A. Richardella, J. Grab, P. Mintun, M. H. Fischer, A. Vaezi, A. Manchon, E.-A. Kim,

- N. Samarth, et al., Spin-transfer torque generated by a topological insulator, Nature **511**, 449 (2014).
- [65] D. Gresta, M. Real, and L. Arrachea, Optimal Thermoelectricity with Quantum Spin Hall Edge States, Phys. Rev. Lett. 123, 186801 (2019).
- [66] A. Badura, W. H. Campos, V. K. Bharadwaj, I. Kounta, L. Michez, M. Petit, J. Rial, M. Leiviskä, V. Baltz, F. Krizek, et al., Observation of the anomalous Nernst effect in altermagnetic candidate Mn₅Si₃, arXiv:2403.12929 https://doi.org/10.48550/arXiv.2403.12929 (2024).
- [67] C. Sürgers, G. Fischer, W. H. Campos, A. B. Hellenes, L. Šmejkal, J. Sinova, M. Merz, T. Wolf, and W. Wernsdorfer, Anomalous Nernst effect in the noncollinear antiferromagnet Mn₅Si₃, Commun. Mater. 5, 176 (2024).
- [68] L. Du, X. Li, W. Lou, G. Sullivan, K. Chang, J. Kono, and R.-R. Du, Evidence for a topological excitonic insulator in InAs/GaSb bilayers, Nat. Commun. 8, 1971 (2017).
- [69] M. Syperek, R. Stühler, A. Consiglio, P. Holewa, P. Wyborski, L. Dusanowski, F. Reis, S. Höfling, R. Thomale, W. Hanke, et al., Observation of room temperature excitons in an atomically thin topological insulator, Nat. Commun. 13, 6313 (2022).
- [70] N. Mao, X. Hu, C. Niu, B. Huang, and Y. Dai, Dual topological insulator and insulator-semimetal transition in mirror-symmetric honeycomb materials, Phys. Rev. B 100, 205116 (2019).
- [71] A. H. Castro Neto, F. Guinea, N. M. R. Peres, K. S. Novoselov, and A. K. Geim, The electronic properties of graphene, Rev. Mod. Phys. 81, 109 (2009).
- [72] T. Yamada, V. L. Deringer, R. Dronskowski, and H. Yamane, Synthesis, Crystal Structure, Chemical Bonding, and Physical Properties of the Ternary Na/Mg Stannide Na₂MgSn, Inorg. Chem. 51, 4810 (2012).
- [73] Z. Wang, Y. Sun, X. Q. Chen, C. Franchini, G. Xu, H. Weng, X. Dai, and Z. Fang, Dirac semimetal and topological phase transitions in A₃Bi (A=Na, K, Rb), Phys. Rev. B 85, 195320 (2012).
- [74] Z. K. Liu, B. Zhou, Y. Zhang, Z. J. Wang, H. M. Weng, D. Prabhakaran, S.-K. Mo, Z. X. Shen, Z. Fang, X. Dai, Z. Hussain, and Y. L. Chen, Discovery of a Three-Dimensional Topological Dirac Semimetal, Na₃Bi, Science 343, 864 (2014).
- [75] See Supplemental Material at [link will be inserted by the publisher] for more details on the $k \cdot p$ method, perturbation techniques and the theory of invariants.
- [76] A. Lau and C. Ortix, Novel topological insulators from crystalline symmetries, Eur. Phys. J. Spec. Top. 227, 1309 (2018).
- [77] E. O. Kane, Band structure of indium antimonide, J. Phys. Chem. Solids 1, 249 (1957).
- [78] K. Shiozaki and M. Sato, Topology of crystalline insulators and superconductors, Phys. Rev. B 90, 165114 (2014).
- [79] P. Blaha, K. Schwarz, F. Tran, R. Laskowski, G. K. Madsen, and L. D. Marks, WIEN2k: An APW+lo program for calculating the properties of solids, J. Chem. Phys. 152, 074101 (2020).
- [80] J. P. Perdew, K. Burke, and M. Ernzerhof, Generalized Gradient Approximation Made Simple, Phys. Rev. Lett. 77, 3865 (1996).
- [81] D. J. Singh and L. Nordstrom, *Planewaves, Pseudopotentials, and the LAPW method* (Springer Science &

- Business Media, 2006).
- [82] G. F. Koster, J. O. Dimmock, R. G. Wheeler, and H. Statz, Properties of the thirty-two point groups (The M.I.T. Press, 1963) p. 138.
- [83] M. Newville, T. Stensitzki, D. B. Allen, and A. Ingargiola, LMFIT: Non-Linear Least-Square Minimization and Curve-Fitting for Python (2015).
- [84] P. E. Faria Junior, T. Campos, C. M. O. Bastos, M. Gmitra, J. Fabian, and G. M. Sipahi, Realistic multiband k · p approach from ab initio and spin-orbit coupling effects of InAs and InP in wurtzite phase, Phys. Rev. B 93, 235204 (2016).
- [85] X. L. Qi, Y. S. Wu, and S. C. Zhang, Topological quantization of the spin Hall effect in two-dimensional paramagnetic semiconductors, Phys. Rev. B 74, 085308 (2006).
- [86] D. Sticlet, F. Piéchon, J. N. Fuchs, P. Kalugin, and P. Simon, Geometrical engineering of a two-band Chern insulator in two dimensions with arbitrary topological index, Phys. Rev. B 85, 165456 (2012).
- [87] B. Göbel, I. Mertig, and O. A. Tretiakov, Beyond skyrmions: Review and perspectives of alternative magnetic quasiparticles, Phys. Rep. 895, 1 (2021).
- [88] N. Nagaosa and Y. Tokura, Topological properties and dynamics of magnetic skyrmions, Nat. Nanotechnol. 2013 812 8, 899 (2013).
- [89] L. Camosi, N. Rougemaille, O. Fruchart, J. Vogel, and S. Rohart, Micromagnetics of antiskyrmions in ultrathin films, Phys. Rev. B 97, 134404 (2018).
- [90] J. Müller, Magnetic Skyrmions and Topological Domain Walls, Ph.D. thesis, Universität zu Köln (2018).
- [91] D. J. Thouless, M. Kohmoto, M. P. Nightingale, and M. den Nijs, Quantized Hall Conductance in a Two-Dimensional Periodic Potential, Phys. Rev. Lett. 49, 405 (1982).
- [92] H. Li, L. Sheng, D. N. Sheng, and D. Y. Xing, Chern number of thin films of the topological insulator Bi₂Se₃, Phys. Rev. B 82, 165104 (2010).
- [93] Y. Yang, Z. Xu, L. Sheng, B. Wang, D. Y. Xing, and D. N. Sheng, Time-Reversal-Symmetry-Broken Quantum Spin Hall Effect, Phys. Rev. Lett. 107, 066602 (2011).
- [94] L. Sheng, H. C. Li, Y. Y. Yang, D. N. Sheng, and D. Y. Xing, Spin Chern numbers and time-reversal-symmetrybroken quantum spin Hall effect, Chinese Phys. B 22, 067201 (2013).
- [95] Q. X. Lv, Y. X. Du, Z. T. Liang, H. Z. Liu, J. H. Liang, L. Q. Chen, L. M. Zhou, S. C. Zhang, D. W. Zhang, B. Q. Ai, H. Yan, and S. L. Zhu, Measurement of Spin Chern Numbers in Quantum Simulated Topological Insulators, Phys. Rev. Lett. 127, 136802 (2021).
- [96] J. Liu, X. Qian, and L. Fu, Crystal Field Effect Induced Topological Crystalline Insulators in Monolayer IV-VI Semiconductors, Nano Lett. 15, 2657 (2015).
- [97] H. Wang, N. Mao, C. Niu, S. Shen, M.-H. Whangbo, B. Huang, and Y. Dai, Ferromagnetic dual topological insulator in a two-dimensional honeycomb lattice, Materials Horizons 7, 2431 (2020).
- [98] Y. Bai, L. Cai, N. Mao, R. Li, Y. Dai, B. Huang, and C. Niu, Doubled quantum spin hall effect with highspin chern number in α-antimonene and α-bismuthene, Phys. Rev. B 105, 195142 (2022).
- [99] G. Bastard, Wave Mechanics Applied to Semiconductor Heterostructures (Editions de physique, Les Ulis, 1990)

- p. 363.
- [100] P. Michetti; P. H. Penteado; J. C. Egues; P. Recher, Helical edge states in multiple topological mass domains, Semicond. Sci. Technol 27, 124007 (2012).
- [101] D. R. Candido, M. Kharitonov, J. C. Egues, and E. M. Hankiewicz, Paradoxical extension of the edge states across the topological phase transition due to emergent approximate chiral symmetry in a quantum anomalous Hall system, Phys. Rev. B 98, 161111(R) (2018).
- [102] J. Zanon, Estados de borda em junções de isolantes topológicos 2D e ferromagnetos: textura de spin e espectro, Masters dissertation, Universidade de São Paulo (2021).
- [103] C.-X. Liu, X.-L. Qi, X. Dai, Z. Fang, and S.-C. Zhang, Quantum Anomalous Hall Effect in Hg_{1-y}Mn_yTe Quantum Wells, Phys. Rev. Lett. 101, 146802 (2008).
- [104] D. G. Rothe, R. W. Reinthaler, C. X. Liu, L. W. Molenkamp, S. C. Zhang, and E. M. Hankiewicz, Fingerprint of different spin-orbit terms for spin transport in HgTe quantum wells, New J. Phys. 12, 065012 (2010).
- [105] V. Krueckl and K. Richter, Switching spin and charge between edge states in topological insulator constrictions, Phys. Rev. Lett. 107, 086803 (2011).
- [106] P. M. Ostrovsky, I. V. Gornyi, and A. D. Mirlin, Symmetries and weak localization and antilocalization of Dirac fermions in HgTe quantum wells, Phys. Rev. B 86, 125323 (2012).
- [107] L. Ortiz, R. A. Molina, G. Platero, and A. M. Lunde, Generic helical edge states due to rashba spin-orbit coupling in a topological insulator, Phys. Rev. B 93, 205431 (2016).
- [108] M. König, H. Buhmann, L. W. Molenkamp, T. Hughes, C. X. Liu, X. L. Qi, and S. C. Zhang, The quantum spin Hall effect: Theory and experiment, J. Phys. Soc. Jpn. 77, 031007 (2008).
- [109] F. Lu, Y. Zhou, J. An, and C. D. Gong, Transversal propagation of helical edge states in quantum spin Hall systems, Europhys. Lett. 98, 17004 (2012).
- [110] B. Zhou, H. Z. Lu, R. L. Chu, S. Q. Shen, and Q. Niu, Finite size effects on helical edge states in a quantum spin-hall system, Phys. Rev. Lett. 101, 246807 (2008).
- [111] C. Liu, T. L. Hughes, X. L. Qi, K. Wang, and S. C. Zhang, Quantum spin hall effect in inverted type-II semiconductors, Phys. Rev. Lett. 100, 236601 (2008).
- [112] Y. Xu, Y. R. Chen, J. Wang, J. F. Liu, and Z. Ma, Quantized Field-Effect Tunneling between Topological Edge or Interface States, Phys. Rev. Lett. 123, 206801 (2019).
- [113] C. Cohen-Tannoudji, B. Diu, and F. Laloë, Quantum Mechanics, Volume 1: Basic Concepts, Tools, and Applications (Wiley, 2019).
- [114] J. J. Sakurai and J. Napolitano, Mod. Quantum Mech., 2nd ed. (Cambridge University Press, 2017) p. 570.
- [115] C. K. Chiu, J. C. Y. Teo, A. P. Schnyder, and S. Ryu, Classification of topological quantum matter with symmetries, Rev. Mod. Phys. 88, 035005 (2016).
- [116] Z. Gao, M. Hua, H. Zhang, and X. Zhang, Classification of stable Dirac and Weyl semimetals with reflection and rotational symmetry, Phys. Rev. B 93, 205109 (2016).
- [117] D. Varjas, T. Rosdahl, and A. R. Akhmerov, Qsymm: algorithmic symmetry finding and symmetric Hamiltonian generation, New J. Phys. 20, 093026 (2018).